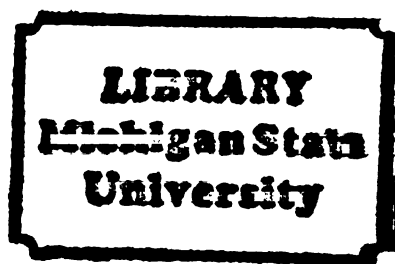


THESIS



This is to certify that the

thesis entitled

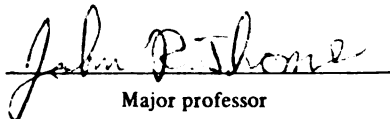
ENHANCED NUCLEATE BOILING

presented by

JAVED ARSHAD

has been accepted towards fulfillment
of the requirements for

M.S. degree in Mechanical Engineering


Major professor

Date 10/15/82



RETURNING MATERIALS:

Place in book drop to
remove this checkout from
your record. FINES will
be charged if book is
returned after the date
stamped below.

--	--	--

ENHANCED NUCLEATE BOILING

By

Javed Arshad

A THESIS

Submitted to
Michigan State University
in partial fulfillment of the requirements
for the degree of

MASTER OF SCIENCE

DEPARTMENT OF MECHANICAL ENGINEERING

1982

ABSTRACT

ENHANCED NUCLEATE BOILING

By
Javed Arshad

The heat transfer mechanism responsible for the order of magnitude increase in the boiling heat transfer coefficient for enhanced boiling surfaces compared to plain smooth surfaces has been investigated experimentally. A video tape recorder and a motor-driven still camera were used to observe the evaporation process in grooves of three cross-sectional geometries with a cover plate over the grooves containing microdrilled holes. Inception of boiling, formation of a thin liquid evaporation layer and dry-out were observed in the groove. It was concluded that thin film evaporation is the principal heat transfer mechanism in nucleate boiling on enhanced surfaces as suggested by several previous investigators. Dry-out of the groove explained the test surface's reversion to the smooth surface pool boiling curve at intermediate heat fluxes.

TABLE OF CONTENTS

LIST OF TABLES	iv
LIST OF FIGURES	v
LIST OF SYMBOLS	xi
1.0 INTRODUCTION	1
2.0 STATE-OF-THE-ART REVIEW	3
2.1 Preliminary work	3
2.2 Nucleation criteria and cavity geometry	3
2.3 Mechanism of heat transfer in nucleate boiling	9
2.4 Commercial enhanced surfaces	13
2.5 Analytical work	15
3.0 EXPERIMENTAL DESIGN AND PROCEDURES	27
3.1 Pool boiling	27
3.2 Visualization experimental design and procedures ...	36
4.0 RESULTS AND DISCUSSION	38
4.1 Pool boiling curves	38
4.2 Visualization of the evaporation phenomenon inside the grooves	46
4.3 Thin film evaporation	55
4.4 Comments	69
5.0 CONCLUSION	70
APPENDICES	71
LIST OF REFERENCES	78

LIST OF TABLES

1. Structural dimensions of the tested surfaces [17]	19
2. Structural dimensions of the test surfaces	30
3. Data for the first pool boiling curve for smooth surface	71
4. Data for the second pool boiling curve for smooth surface	72
5. Data for the first pool boiling curve for enhanced Surface No. 1	73
6. Data for the second pool boiling curve for enhanced Surface No. 1	74
7. Data for the first pool boiling curve for enhanced Surface No. 2	75
8. Data for the second pool boiling curve for enhanced Surface No. 2	76

LIST OF FIGURES

1.	Effect of emery paper roughening for acetone boiling on copper [3]	4
2.	(a) States of the liquid-vapor interface in a reentrant cavity. (b) Reciprocal ($1/r$) vs. vapor volume for liquid having a 90° contact angle [6]	7
3.	(a) Effect of several surface treatments on sodium boiling at 65 mm Hg [7]. (b) Cross section of doubly reentrant cavities tested	8
4.	(a) Enhancement for water boiling at 101 kPa (1 atm) on a stainless steel surface having minute nonwetted spots (30-60 spots/cm ² , 0.25 mm diameter or less). (b) Enlarged photo of Teflon-spotted smooth surface [8] ..	10
5.	A typical photograph of the oscilloscope face showing the surface temperature behavior [13]	12
6.	Sketches of two ways the microlayer might vaporize	12
7.	(a) Cross section of copper sintered porous boiling surface. (b) Enhancement provided by porous HIGH-FLUX surface for three fluids boiling at 101 kPa (1 atm) [14]	14
8.	Some patented boiling surfaces applied to circular tubes [1]	16-17
9.	Comparative single-tube pool boiling test results for p-xylene at 101 kPa (1 atm). From [16]	18
10.	Geometry of the surface structure [17]	19
11.	Boiling curves of water [17]	21
12.	Contribution of latent heat transport to total heat flux [17]	21
13.	Apparatus for observation experiment [17]	22

14. Comparison between the measured heat flux and the predicted heat flux for water and nitrogen [17]	22
15. Measured boiling data of 14 fluids on HIGH-FLUX sintered surface compared with values predicted by Eq. (2-12) [14]	26
16. Magnified view of the surface [17]	28
17. Test surface; (a) Side View, (b) Top View (c) and (d) Groove cross-sections	29-30
18. U-tube pool boiling facility	32
19. Power supply circuit	33
20. Visualization experimental setup	37
21. First pool boiling curve for the smooth surface	39
22. Second pool boiling curve for smooth surface	40
23. First pool boiling curve for Surface No. 1	41
24. Second pool boiling curve for Surface No. 1	42
25. First pool boiling curve for Surface No. 2	43
26. Second pool boiling curve for Surface No. 2	44
27. Pool boiling curves	45
28. Schematic sequence of activation of a vapor pocket and film dryout at medium heat flux	48
29. Schematic of shape of film in three geometries	49
30. (T1) Evaporation starts from right corner	51
31. (T1) Vapor front advancing in the groove	51
32. (T1) Vapor starts coming out of the groove, liquid inside forms of a film on the groove walls	52
33. (T1) At low heat flux liquid film is apparent	52
34. (T1) At intermediate heat flux lower half of the groove seems to have dried-out	53
35. (T1) Flooded groove	53

36. (T1) Liquid-vapor front in the groove as the heating is stopped and groove is getting flooded	54
37. (T1) Groove flooding	54
38. (T2) Flooded groove	56
39. Evaporation starts in the groove	56
40. Vapor starting to come out through the pore	57
41. Liquid forms a film on groove walls	57
42. Nucleation at lower heat flux	58
43. Nucleating groove at intermediate heat flux	58
44. (R1) Flooded groove	59
45. (R1) Evaporation starting from lower right corner	59
46. (R1) Vapor front advancing in the groove	60
47. (R1) Liquid being pushed out of the groove	60
48. (R1) Nucleating groove at lower heat flux	61
49. (R1) Nucleating groove at intermediate heat flux	61
50. (R1) Nucleating groove at intermediate heat flux	62
51. (R1) Nucleating groove (higher heat flux), liquid film is less apparent	62
52. (C1) Flooded groove	63
53. (C1) Nucleating groove (a uniform thin film is seen along the periphery). Low heat flux is applied	63
54. (C1) Nucleating groove (low heat flux)	64
55. (C1) Groove flooding as the liquid-vapor front moves in when heating is stopped	64
56. (C2) Flooded groove	65
57. (C2) Nucleating groove	65
58. (C2) Nucleating groove (intermediate heat flux)	66
59. (C2) Nucleating groove (low heat flux). Droplets in groove and bubble are formed by condensation on the glass plates	66

60.	(C2) Groove flooding	67
61.	(C2) Evaporation starting at different spots along the periphery	67

List of Symbols

Nomenclature

A	area [m^2]
d_b	bubble departure diameter [m]
h	heat transfer coefficient [$\text{W}/(\text{m}^2\text{K})$]
h_{fg}	heat of vaporization [J/kg]
k	thermal conductivity [$\text{kW}/\text{m}\text{--}^\circ\text{C}$]
m	slope of vapor pressure curve
N_A	number of active boiling sites
P	pressure [N/m^2]
q	heat flux [W/m^2]
q_{ex}	heat flux on the outer surface [W/m^2]
r	cavity mouth radius [m]
T	temperature [$^\circ\text{C}$]
V_{fg}	volume of vaporization [m^3/Kg]
σ	surface tension [dyne/m]

Subscripts

L	latent
l	liquid
max	maximum
opt	optimum
sat	saturation
V	vapor
w	wall

1.0 INTRODUCTION

Heat transfer enhancement has received much attention recently, in part due to rising energy costs. The heat transfer enhancement techniques are employed to economize on equipment cost and size, handling large and concentrated heat fluxes and improving the performance of the heat exchange equipment. Special enhanced boiling surfaces, now largely in use for building heat exchange equipment, incorporate a special surface microgeometry which promotes high performance nucleate boiling with heat transfer coefficients an order of magnitude greater than those of a conventional smooth surface.

On a typical pool boiling curve when entering the boiling region from natural convection there is a large increase in the heat transfer coefficient. Two mechanisms are basically responsible for this increase: latent heat transport in the form of bubbles leaving the nucleating surface and agitation caused by growing and departing bubbles enhancing natural convection over the inactive area.

Enhanced boiling surfaces are a 5 to 10 fold improvement (in terms of heat transfer coefficients) over conventional smooth surfaces for moderate heat fluxes up to about 200 kW/m^2 . A number of different techniques have been employed to prepare these special surfaces. In the early investigations surfaces roughened with different grades of emery paper were tested. These surfaces showed a temporary improvement before reverting to smooth surface behavior. The later investigations concentrated more on

artificially formed nucleation sites whose performance did not deteriorate with time. These surfaces with a high population density of stable nucleation sites are commercially available under different trademarks. A high performance of these special surfaces has been thought to be due a) to a lower superheat required for initiation of boiling because of large radii of the vapor nuclei trapped in the cavities of special geometry b) to a high density of such boiling sites and c) to thin film evaporation within the structured porous matrix.

Although a number of researchers have manufactured and tested a variety of enhanced surfaces, only a very few have done a detailed study of the heat transfer mechanism responsible for the order of magnitude increase in the boiling heat transfer coefficient for enhanced surfaces. Such a study is vital before we can model the boiling process to look for an analytical expression for predicting the heat transfer coefficient.

In the present study two special surfaces were designed and manufactured. These surfaces had grooves machined into them (one surface with triangular cross-sectional grooves and the other with rectangular) and a cover plate containing microdrilled holes placed over the grooved surface. Nucleate pool boiling curves were obtained to ascertain the performance of these two surfaces compared to a plain smooth surface. In a separate set up for a visual study, a videotape recorder and a motor-driven still camera were used to observe the evaporation process in grooves of three different cross-sectional geometries (triangular, rectangular and circular).

Chapter 2 deals with the state-of-the-art review of enhanced boiling. Chapter 3 describes the experimental design and procedures for the present study followed by a discussion of the results in Chapter 4. Chapter 5 presents the conclusions of the study.

2.0 STATE-OF-THE-ART REVIEW

2.1 Preliminary work

Previous investigators have tested heat transfer surfaces incorporating a wide variety of enhancement techniques. An excellent and recent review by Webb [1] describes the historical development and testing of these surfaces for a wide range of liquids.

Early investigators [2,3] tested several liquids on surfaces roughened with different grades of emery paper. However, only a temporary improvement was shown before the surface behavior reverted back to that of a conventional smooth surface. Khurihari and Myer's [3] results (see Figure 1) showed that the heat transfer coefficient was proportional to the surface roughness. They noted that boiling site density (the number of boiling sites per unit area) increased with increasing roughness. The later investigators concentrated more on artificially formed nucleation sites whose performance would not deteriorate with time. The artificially formed sites also allowed incipience to occur at a lower degree of wall superheat, ΔT , which is the temperature difference between the heated wall and the bulk liquid temperature.

2.2 Nucleation criteria and cavity geometry

Bankoff [4] examined the mechanism of bubble nucleation in detail and arrived at the conclusion that boiling bubbles originate from pre-existing vapor pockets in cavities on the surface. Westwater [5] exa-

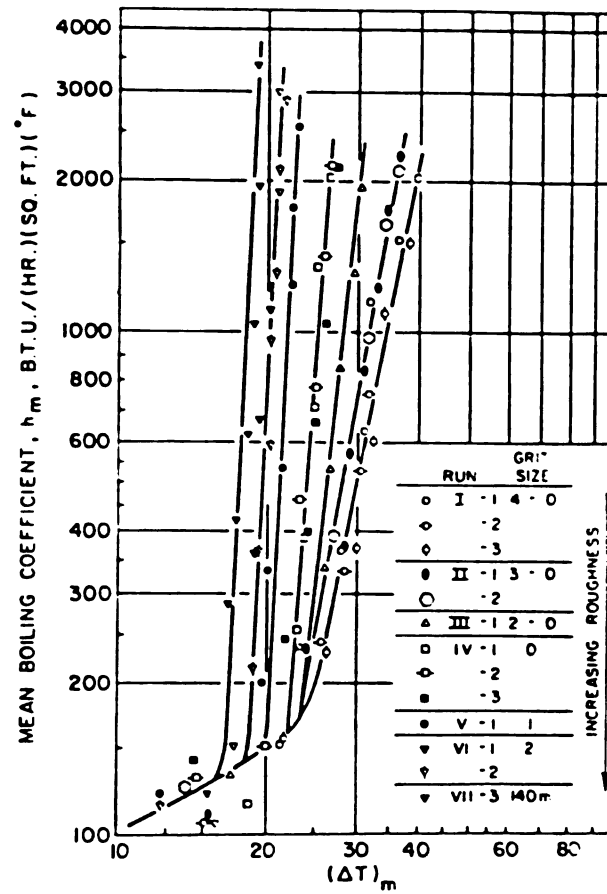


Figure 1. Effect of emery paper roughening for acetone boiling on copper [3].

mined the boiling surface under a microscope and confirmed Bankoff's conclusion.

Griffith and Wallis [6] made a detailed study of boiling from artificially formed sites. They correlated their observations with the following nucleation criteria.

The Gibb's equation for a static, mechanical equilibrium across a curved interface which is a segment of a sphere can be written as

$$P_v - P_l = \Delta P = \frac{2\sigma}{r} \quad (2-1)$$

When the bubble is also in a state of thermal equilibrium the temperature of the vapor inside the bubble must be identical to that of the surrounding liquid. Now the vapor is at its saturation temperature corresponding to P_v . Since $P_v > P_l$, the liquid surrounding the bubble must be superheated. The excess temperature in the liquid can be related to the pressure difference ΔP through the Clapyron equation.

The Clapeyron equation is given as

$$\frac{\Delta P}{\Delta T} = \frac{h_{fg}}{T_{sat} V_{fg}} \quad (2-2)$$

Eliminating ΔP from eqs. (2-1) and (2-2) we get

$$(T_w - T_{sat}) = \Delta T = \frac{2\sigma T_{sat} V_{fg}}{r h_{fg}} \quad (2-3)$$

If the cavity mouth radius r , also called the critical radius, is substituted into eq. (2-3), the temperature difference (ΔT) becomes the nucleation superheat. This is the minimum wall superheat needed to start the bubble growing from a cavity with a mouth radius of r .

Griffith and Wallis [6] compared the experimental values of ΔT (nucleation superheat) for different artificial cavities with those calculated from eq. (2-3). The results showed that the nucleation criteria embodied in eq. (2-3) are correct. In one of their tests on artificial cavities they noted that the measured wall superheat was 20°F (11°C) as opposed to 3°F (1.7°C) as calculated from eq. (2-3). To explain this they argued that the mean surface temperature is not equal to the temperature felt by an active cavity i.e., the surface is much cooler in the vicinity of an active cavity than elsewhere. They concluded that the cavity mouth radius determines the wall superheat needed to initiate boiling and its shape determines its stability once boiling has begun. Figure 2(a) shows a reentrant cavity proposed by Griffith and Wallis. It is called "reentrant" because of its special internal shape. Figure 2(b) shows a plot of the reciprocal of radius vs. volume. When the radius of curvature becomes negative, then according to eq. (2-3), the liquid must be subcooled in order to flood the cavity. Therefore, such a cavity should be a very good vapor trap to serve as a nucleation site for the initiation of boiling.

Marto and Rohsenow [7] conducted their tests on a 75mm diameter block with twelve reentrant cavities. Figure 3(b) shows a cross-sectional view of their artificial cavities which produced much better enhancement in terms of heat transfer coefficient compared to some other enhancement techniques they tested (see their results Figure 3(a)).

Hummel [8] tested a stainless steel surface sprayed with scattered spots of teflon (a non wetting material) for the boiling of water. A nonwetting coating establishes a larger liquid-vapor interfacial curvature which in turn would require a lesser degree of superheat for its

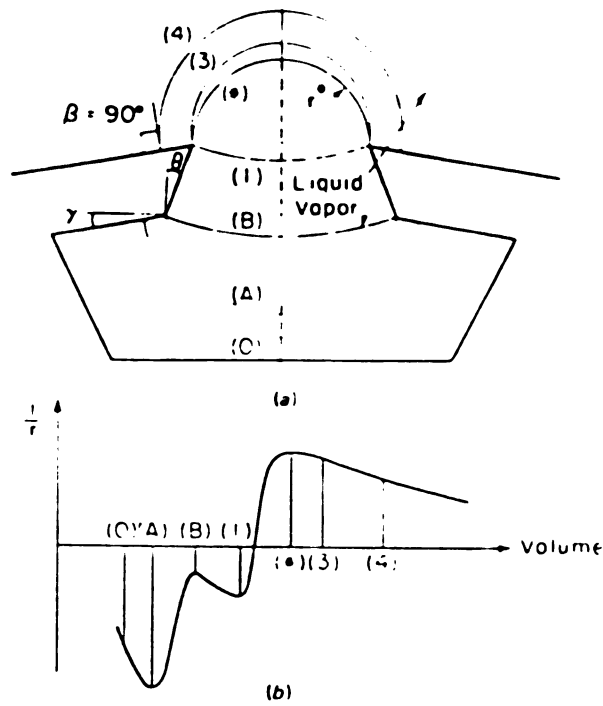


Figure 2. (a) States of the liquid-vapor interface in a reentrant cavity. (b) Reciprocal ($1/r$) vs. vapor volume for liquid having a 90° contact angle [6].

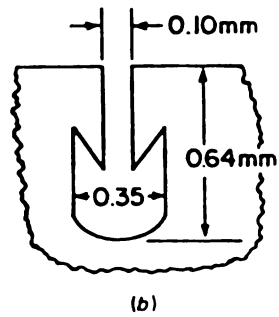
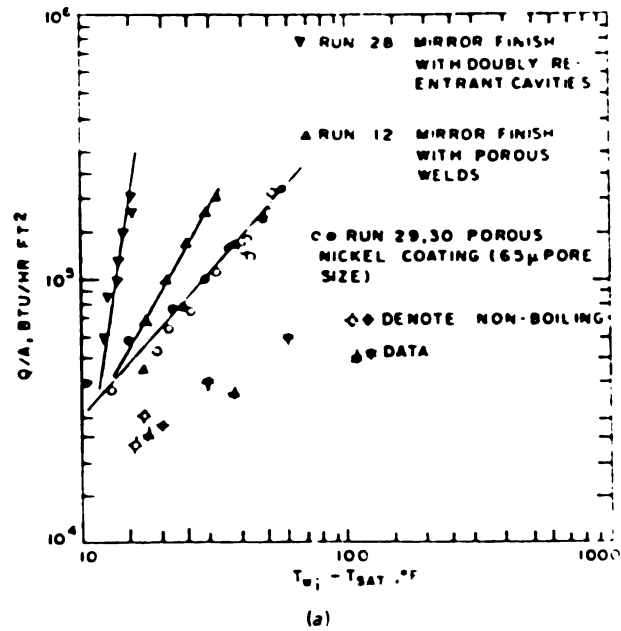


Figure 3. (a) Effect of several surface treatments on sodium boiling at 65 mm Hg [7]. (b) Cross section of doubly reentrant cavities tested.

existence. Hummel's results (see Figure 4) show a dramatic enhancement where h increases an order of magnitude for a given ΔT .

2.3 Mechanisms of heat transfer in nucleate boiling

There are several hypothesis about the mechanism of heat transfer in boiling. First, a growing bubble is thought to be surrounded by a superheated thermal boundary layer. Heat is absorbed by the bubble from this boundary layer on its periphery and the heat is transported away as the bubble departs from the heated surface.

Another mechanism is known as thermal boundary layer stripping. Adjacent to the heated surface a thermal boundary layer exists in the fluid. Heat is thought to be transported by cyclic stripping of the thermal boundary layer by departing bubbles. Also, as the bubbles leave the surface, they allow the cold liquid to contact the surface. The cold liquid readily conducts heat away from the hot surface. Such a mechanism appears to be more dominant in subcooled boiling as shown by Rohsenow and Clark [9]. The above ideas are also shared by a number of other researchers [10,11].

Yet another hypothesis is that the liquid at the base of a bubble is rapidly vaporized, as advocated by Edwards [12] and Moore and Mesler [13]. They visualize that evaporation takes place continuously from a thin liquid film at the base of the bubble. The temperature of such a film would be expected to drop significantly after the mass transfer has begun due to the associated very high heat transfer coefficient for thin film evaporation (similar to film condensation).

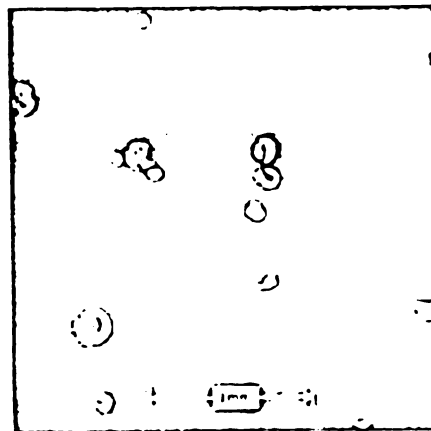
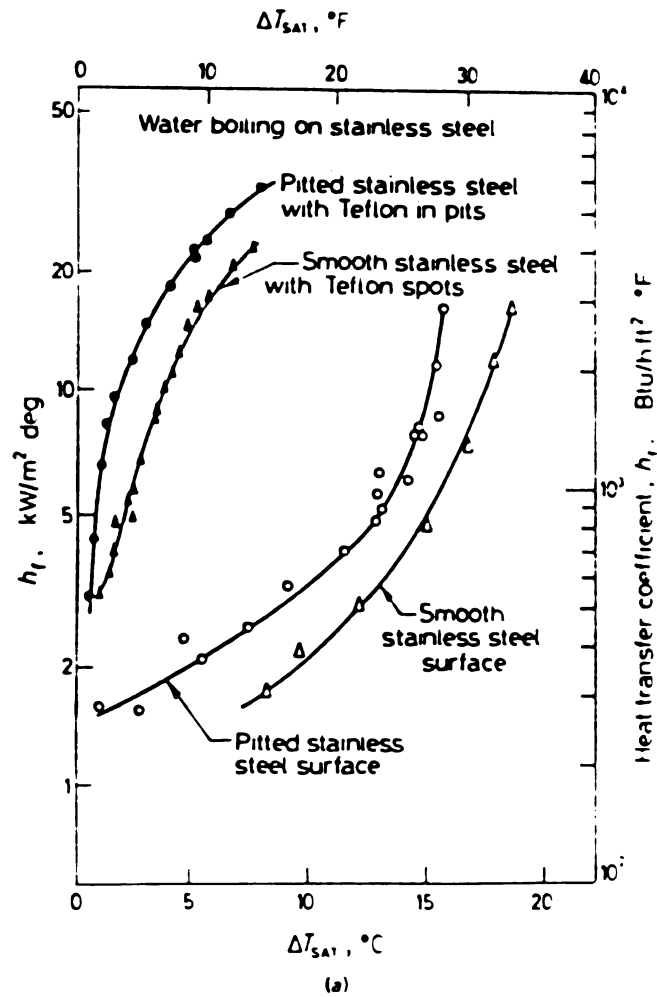


Figure 4. (a) Enhancement for water boiling at 101 kPa (1 atm) on a stainless steel surface having minute nonwetted spots (30-60 spots/cm², 0.25 mm diameter or less). (b) Enlarged photo of Teflon-spotted smooth surface [8].

Moore and Mesler [13] measured the surface temperature during nucleate boiling with a special thermocouple so designed as to measure the surface temperature of a small area and to have an extremely rapid response time. The thermocouple voltage was read on a potentiometer and the temperature fluctuations were viewed on an oscilloscope. The surface temperature was found to drop occasionally by 20 to 30°F (11 to 17°C) in about 2 milliseconds and then return to its previous level during the boiling of water. This indicated a rapid extraction of heat during a short time interval. Figure 5 shows a typical photograph of the oscilloscope face showing the surface temperature behavior.

Moore and Mesler calculated the heat transfer rate during one temperature drop and then multiplied it with the frequency of the temperature drop and showed that it accounted for about 70-90% of the average heat flux for many calculations. They also argued that the very high heat transfer coefficient (between 165-267 kW/m²°C) obtained during the temperature excursion would not be expected if convection was an important factor. They proposed that the only hypothesis that appears to be consistent with their observations is the process of vaporization at the base of the bubble. They visualize the details of what happens as follows. As a bubble grows on the surface it exposes the heating surface wet with a microlayer of liquid to the interior of the bubble. This microlayer rapidly vaporizes, removing heat rapidly from the surface until it is completely vaporized. This simple sequence of events is the only way that they were able to explain the rapid removal of heat occurring during the short period of time when they observed the surface temperature dropping rapidly. Figure 6 shows two extreme possibilities of bubble growth and the formation of a microlayer. They suggested it might be

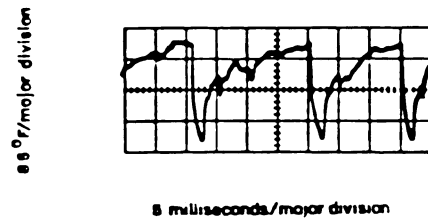


Figure 5. A typical photograph of the oscilloscope face showing the surface temperature behavior [13].

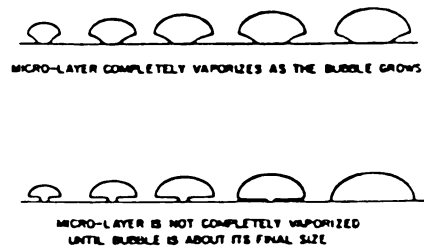


Figure 6. Sketches of two ways the microlayer might vaporize [13].

possible to achieve better correlations if consideration was given to microlayer vaporization.

2.4 Commercial enhanced surfaces

Based on the past experience with special surfaces and the fundamental studies mentioned in the previous sections, a number of techniques have been employed to manufacture a variety of commercial enhanced surfaces.

A category of "porous surfaces" incorporates microholes (pores) connected to a matrix of interconnected reentrant cavities under the surface. These surfaces have proved to be a major breakthrough. Figure 7a shows a cross-section of the HIGH-FLUX* surface which consists of a porous metallic matrix bonded to a metallic substrate. The Gottzmann et. al. [14] results for pool boiling tests on a HIGH-FLUX surface are shown in Figure 7b. At a given heat flux the heat transfer coefficient is seen to increase by a factor of 20 due to the smaller ΔT required by the enhanced surface to sustain the heat flux. The average pore size within a certain range has been reported to be the most significant dimension. Most of these pores are of reentrant shape according to Bergles and Chyu [15]. The pores within a matrix are interconnected such that vapor formed in one pore can activate adjacent pores.

Cold metal working is also one of the techniques being employed to form a high density of interconnected reentrant cavities in the form of grooves or tunnels below the surface. These surfaces have openings all along the top of the grooves connecting them with the bulk liquid. Fig-

*Trademark Union Carbide

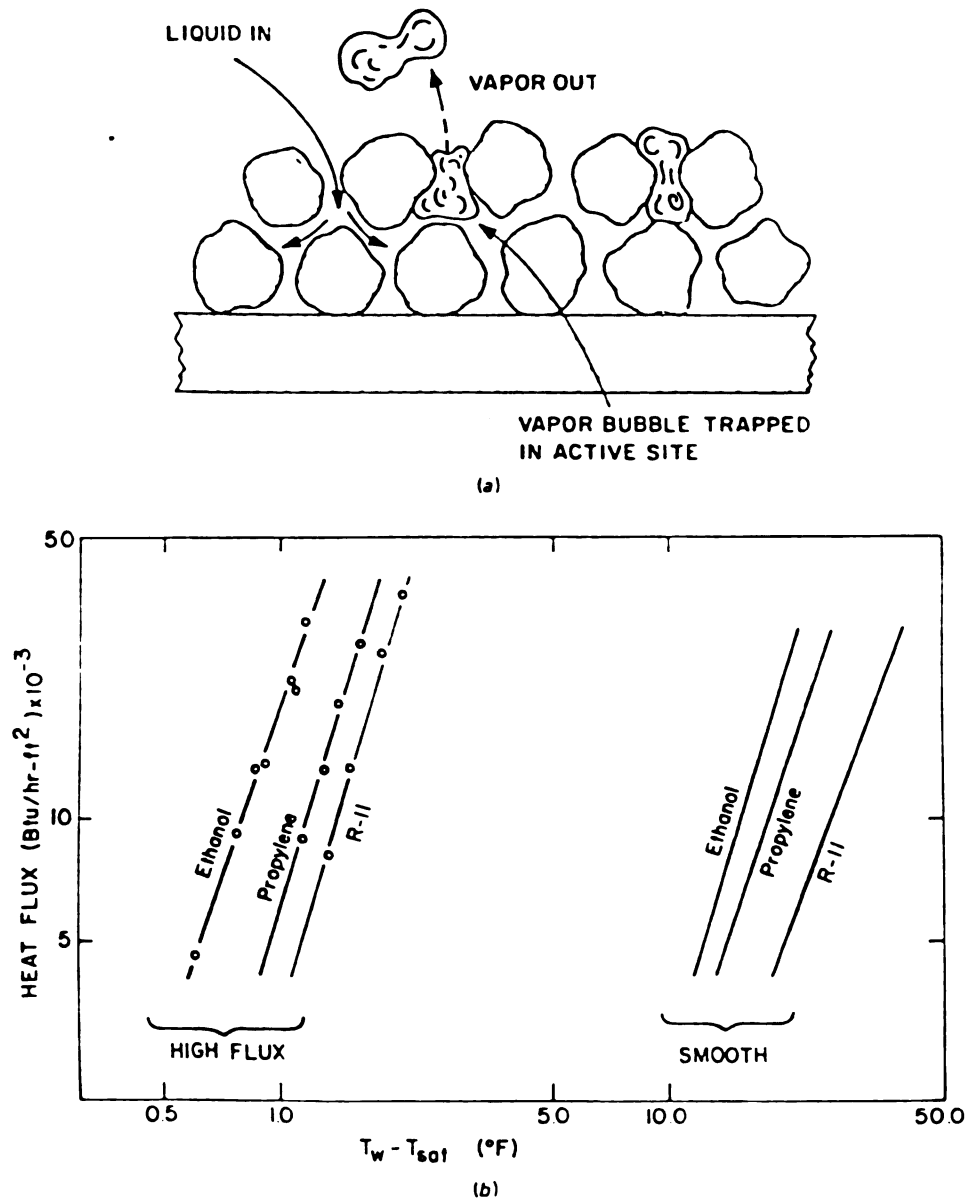


Figure 7. (a) Cross section of copper sintered porous boiling surface. (b) Enhancement provided by porous HIGH-FLUX surface for three fluids boiling at 101 kPa (1 atm) [14].

ure 8 shows some of the commercially available boiling surfaces of this type. Figure 8a depicts a reentrant grooved surface formed by bending fin tips to form narrow cavity openings. Figure 8b shows the THERMO-EXCEL-E (trade mark) surface consisting of reentrant grooves with holes at the top of enclosed grooves. Figure 8c shows the GEWA-T surface consisting of narrow finned tubing with the fins flattened down. Figure 8d is the ECR-40 surface made by cross knurling through helical fins and then compressing the surface to form reentrant cavities.

Yilmaz and Westwater [16] conducted single tube pool boiling tests on some of these commercial enhanced surfaces. Their results are shown in Figure 9. The ECR-40 and the HIGH FLUX surfaces gave the best results. These tubes also exhibited a critical heat flux (CHF) about 40% greater than that of a conventional smooth tube.

2.5 Analytical work

While a variety of enhanced surfaces have been manufactured and tested and are in fact commercially available, very little work has been done to mathematically model the enhancement mechanism to look for some heat transfer correlation for these surfaces.

Nakayama et. al. [17] have proposed an analytical model of the dynamic cycle of bubble formation. They conducted experiments on structured surfaces composed of interconnected internal cavities in the form of tunnels and small pores connecting the bulk pool of liquid and the tunnels. Figure 10 shows the geometry of the structured surface they used in their experiments. Structural dimensions are given in Table 1 for three different surfaces used for boiling water. The surface material was oxygen free copper. The most widely varied among the geometrical dimensions

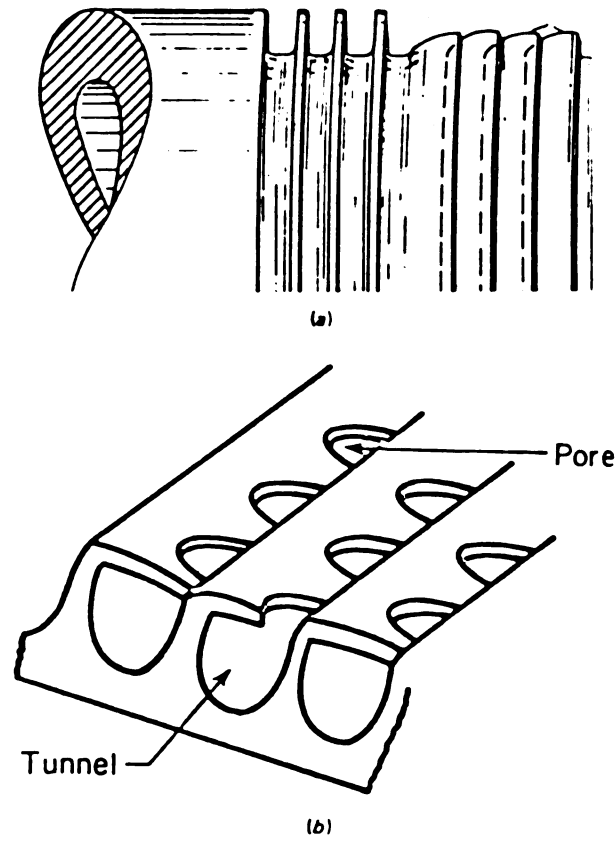
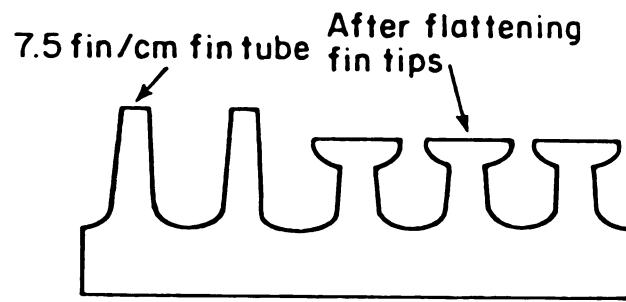
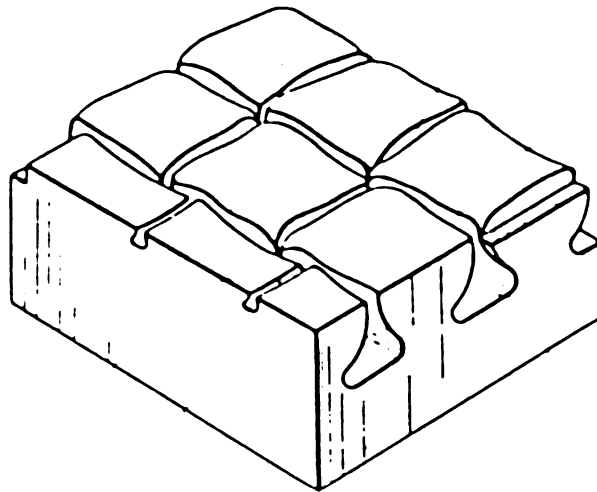


Figure 8. Some patented boiling surfaces applied to circular tubes [1].



(c)



(d)

Figure 8. (continued)

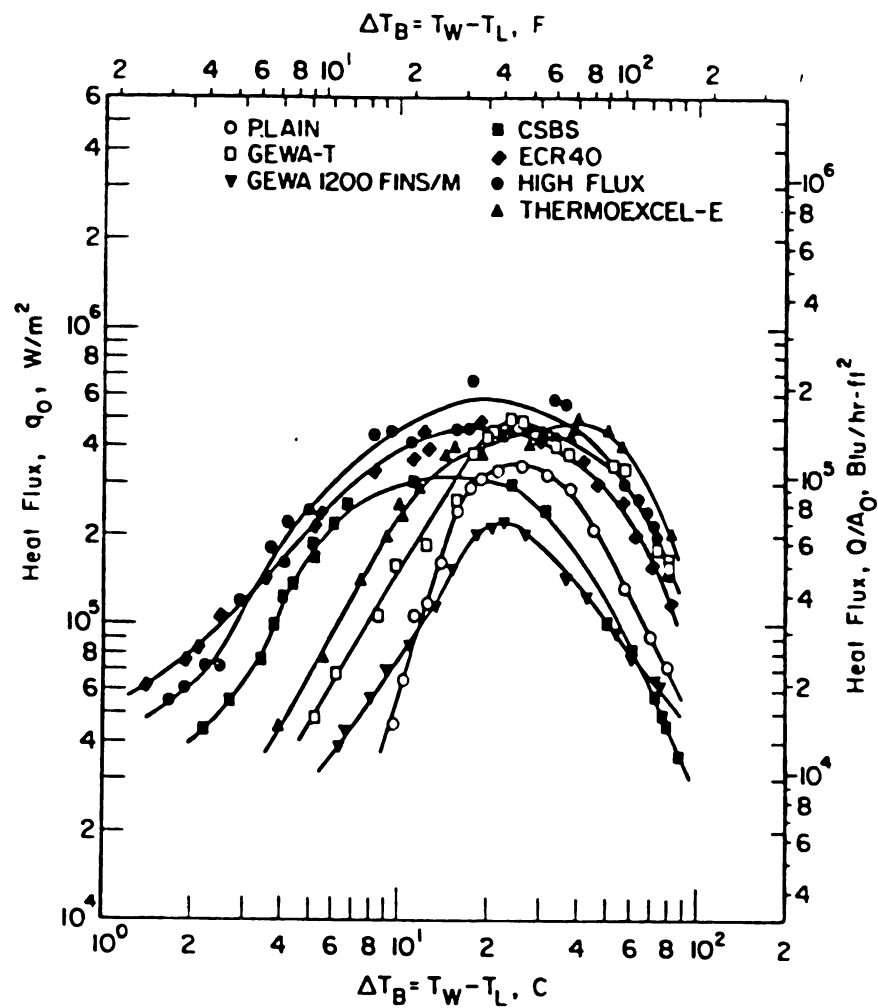


Figure 9. Comparative single-tube pool boiling test results for p-xylene at 101 kPa (1 atm). From [16].

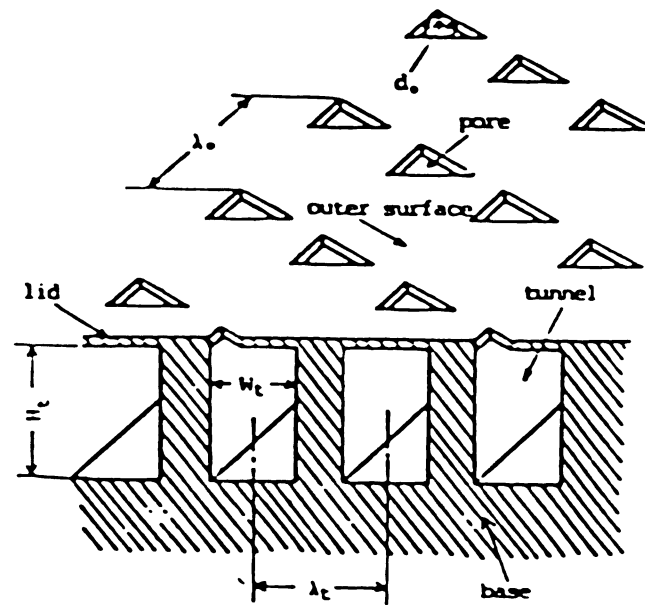


Figure 10. Geometry of the surface structure [17].

Table 1. Structural dimension of the tested surfaces [17].

fluid	Surface No.	d_o	λ_o	λ_t	H_t	W_t	A_t/A
water	W-1	0.20	0.60	0.60	0.62	0.25	2.93
	W-2	0.14	0.72	0.50	0.50	0.20	3.40
	W-3	0.08	0.72	0.50	0.60	0.15	3.70
R-11	R(11)-1	0.10	0.70	0.55	0.40	0.25	3.36
	R(11)-2	0.06	0.70	0.55	0.40	0.25	3.36
	R(11)-3	0.04	0.70	0.55	0.40	0.25	3.36
liquid nitrogen (LN)	LN-1	0.20	0.72	0.40	0.40	0.18	3.33
	LN-2	0.12	0.72	0.40	0.50	0.14	3.71
	LN-3	0.09	0.72	0.40	0.56	0.16	4.05
	LN-4	0.06	0.72	0.40	0.52	0.18	4.05
	LN-5	0.03	0.72	0.40	0.56	0.18	4.09

(mm)

was the pore diameter d_o which was considered crucial for the ejection of vapor bubbles from the tunnel. Boiling curves are shown in Figure 11. Dependence of boiling performance on pore diameter d_o is notable.

To determine the latent heat contribution to the overall heat transfer rate, they measured boiling site density N_A/A , the bubble departure frequency f_b , and the diameter of departing bubbles d_b for R-11. The latent heat flux q_L , was then computed from

$$q_L = (N_A/A) f_b h_{fg} \rho_v (\pi d_b^3/6) \quad (2-4)$$

where ρ_v is vapor density and h_{fg} latent heat of vaporization.

The ratio of q_L to the total heat flux q is shown against q in Figure 12. The latent heat contribution for the structured surface is seen to be dominating at low heat fluxes. This is thought to imply that a significant role is played by the vaporization process in the tunnels.

Nakayama et. al. [17] have also conducted visual experiments to observe the vaporization process in the tunnels. The apparatus shown in Figure 13 consists of a base block, two glass plates (30mm x 30mm, 1mm thick) forming a pool space above the base block, and a thin metal lid having a row of through holes (pores). A tunnel space is formed between the lid and the base block. Heat was supplied through the direct heating of the base block or by passing a d.c. current through the lid. The evaporation phenomenon in the continuous tunnel was observed from the side. Based on their observations and experimental results they modeled a sequence of events of the bubble growth and departure cycle at the pores in an effort to develop an analytical solution to find q_L .

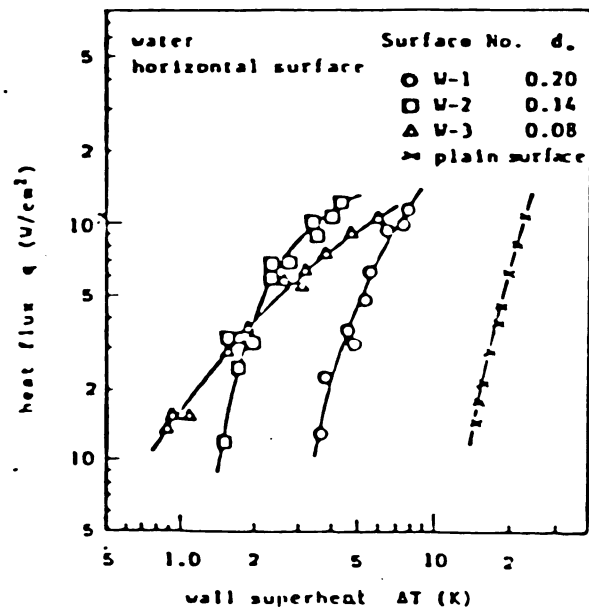


Figure 11. Boiling curves of water [17].

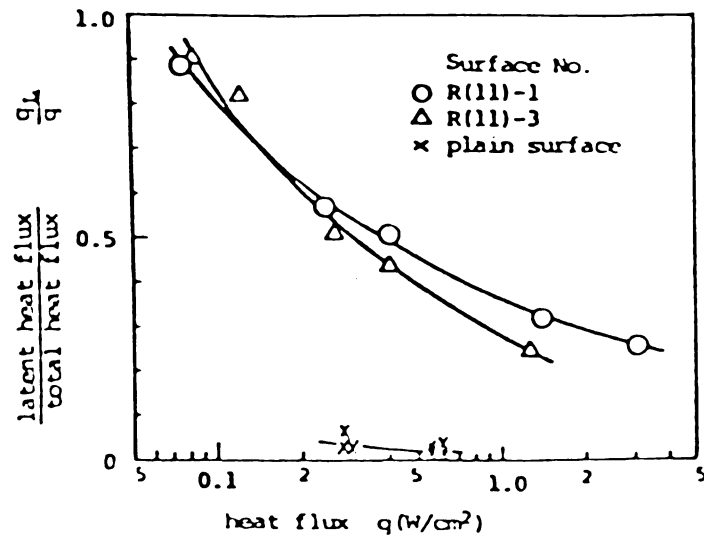


Figure 12. Contribution of latent heat transport to total heat flux [17].

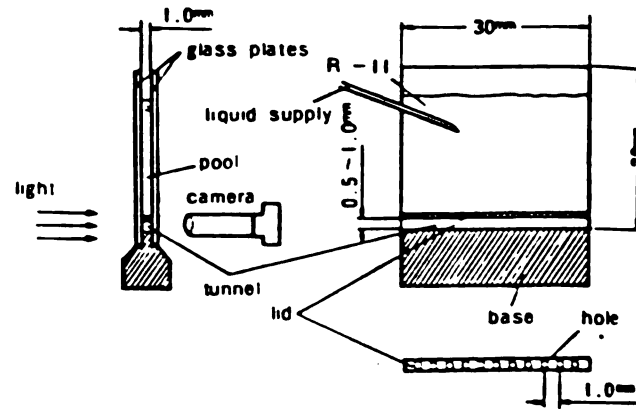


Figure 13. Apparatus for observation experiment [17].

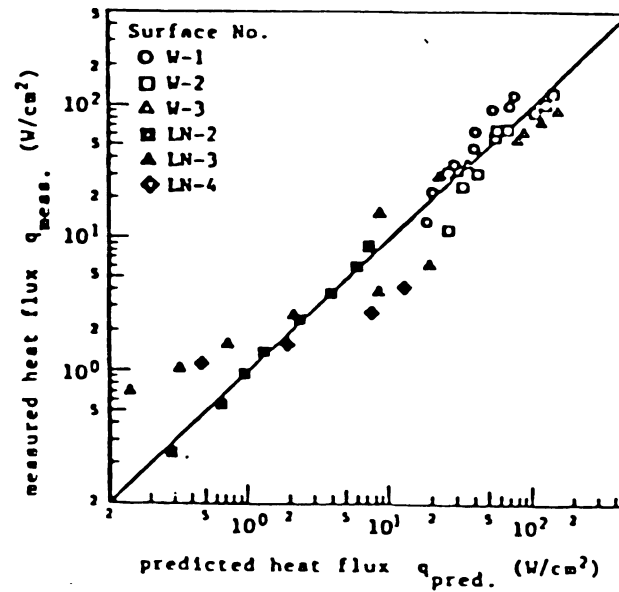


Figure 14. Comparison between the measured heat flux and the predicted heat flux for water and nitrogen [17].

Basically they have made use of conservation equations of mass and momentum in terms of meniscus height at the active and inactive pores. These equations were derived by referring to [18]. They derive expressions for the mass of liquid evaporated in the tunnels, the time for completing a cycle, and the fraction of total number of pores active β . Then, the latent heat transport flux is given as

$$q_L = \frac{\text{mass of liquid}}{\text{(evaporated in tunnels)}} h_{fg} / (\text{Time})(\text{Area}) \quad (2-5)$$

They also gave an empirical correlation for q_{ex} , the heat flux from the outer surface of structured surface.

$$q_{ex} = (\Delta T / C_q)^{1/y} (N_A / A)^{-x/y} \quad (2-6)$$

where x, y and C_q are constants which could vary from one fluid to another and $N_A = \beta N$, where N is the total number of pores. Now

$$q = q_L + q_{ex} \quad (2-7)$$

In the process of arriving at Eq. (2-7) five empirical constants have been introduced to correlated their experimental results (see Figure 14). A procedure of predictive computations for geometrically uniform surface structures (such as their own) is outlined. They noted that more experiments on similar surfaces were necessary to test the validity of their analytical model.

The Gottzmann et. al. [14] model is strongly based on the assumption that effectively all vaporization occurs within the porous matrix or tun-

nels, see Figure 7a. They also make use of Gibb's equation and the well known Clapyron relation;

$$\Delta P = \frac{2\sigma}{r} \quad (2-1)$$

$$\frac{\Delta P}{\Delta T} = \frac{h_{fg}}{T_{sat} v_{fg}} \quad (2-2)$$

where $\Delta T = T_w - T_s$; letting $\frac{\Delta P}{\Delta T} = m$, the slope of the vapor pressure curve and substituting (2-2) in (2-1) gives

$$\Delta T = \frac{2\sigma}{rm} \quad (2-8)$$

Neglecting the temperature drop across the metallic matrix, the total wall superheat ΔT_B will be the sum of ΔT_s , eq. (2-8), and the temperature drop ΔT_{LF} across the thin liquid film covering the metallic walls. Therefore

$$\Delta T_B = \Delta T_s + \Delta T_{LF} \quad (2-9)$$

and

$$\Delta T_B = \frac{2\sigma}{rm} + \frac{\beta q r^2}{k_l} \quad (2-10)$$

where a geometric factor β is introduced. The conduction of heat through the liquid from the hot solid surface to the liquid-vapor interface is called thin film evaporation (It is similar to film condensation).

The optimum radius is found by differentiating eq. (2-10) giving

$$r_{\text{opt.}} = \left(\frac{\sigma k_l}{\beta m q} \right)^{1/3} \quad (2-11)$$

Substituting back into eq. (2-10) gives

$$h_{\text{max}} = \frac{k_l m^2 \Delta T_B^2}{27 \beta \sigma^2} \quad (2-12)$$

Gottzmann tested this equation for several surfaces with optimum pore sizes. Results are shown in Figure 15. The data is seen to be rather scattered but good qualitative agreement is found.

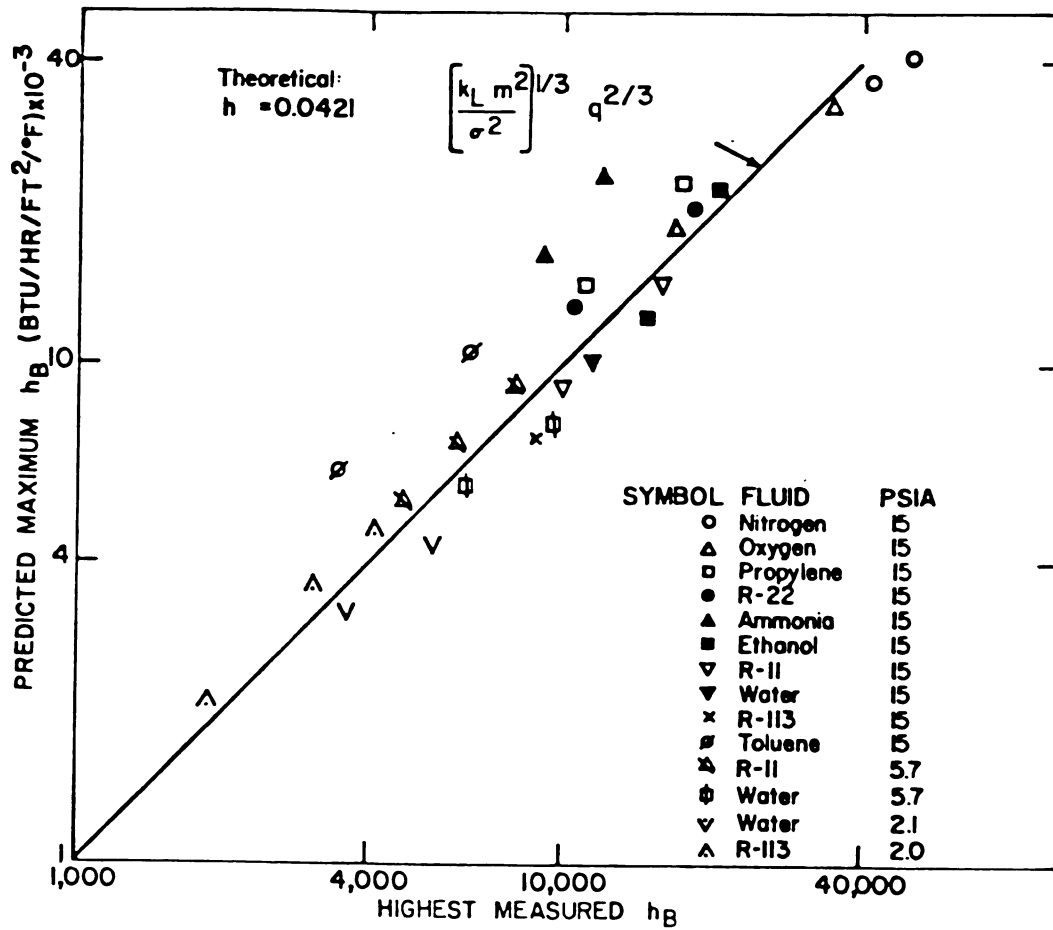


Figure 15. Measured boiling data of 14 fluids on HIGH-FLUX sintered surface compared with values predicted by Eq. (2-12) [14].

3.0 EXPERIMENTAL DESIGN AND PROCEDURES

3.1 Pool boiling

An experimental program was designed to study the enhancement mechanism in porous structured surfaces in continuation of the Nakayama et. al. [17] work. However the exact geometry of the structured surface was known in the present study as opposed by the previous work by Nakayama where the geometry was only approximately rectangular as shown in Figure 16. To study the effect of a change in groove geometry on enhancement, boiling curves for two different groove cross-sections (triangular and rectangular) were obtained.

The two special enhanced boiling test surfaces made of brass were designed, manufactured and tested in the laboratory. The test section (25.4mm dia) contained circular machined grooves: one surface with a triangular cross-section and the other with rectangular, coded surface No. 1 and No. 2 respectively for convenience. A thin copper lid (thickness 5 μ m) was soldered onto the surface which covered the machined grooves forming tunnels. The lid contained microdrilled holes (pores) all along the centerline of the grooves, thus connecting the tunnels with the bulk pool of water. Dimensions were carefully selected to have a uniform distribution of pores over the entire test section.

Figure 17 shows detailed drawings of the test surfaces and Table 2 gives the dimensions of the surface structures. The outer section of the test surface was made very thin (0.4mm) to minimize the conduction heat

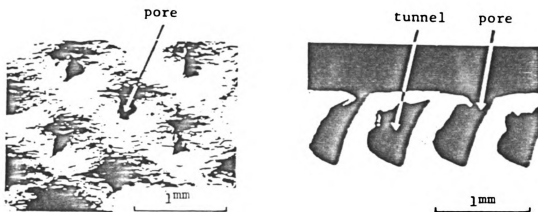


Figure 16. Magnified view of the surface [17].

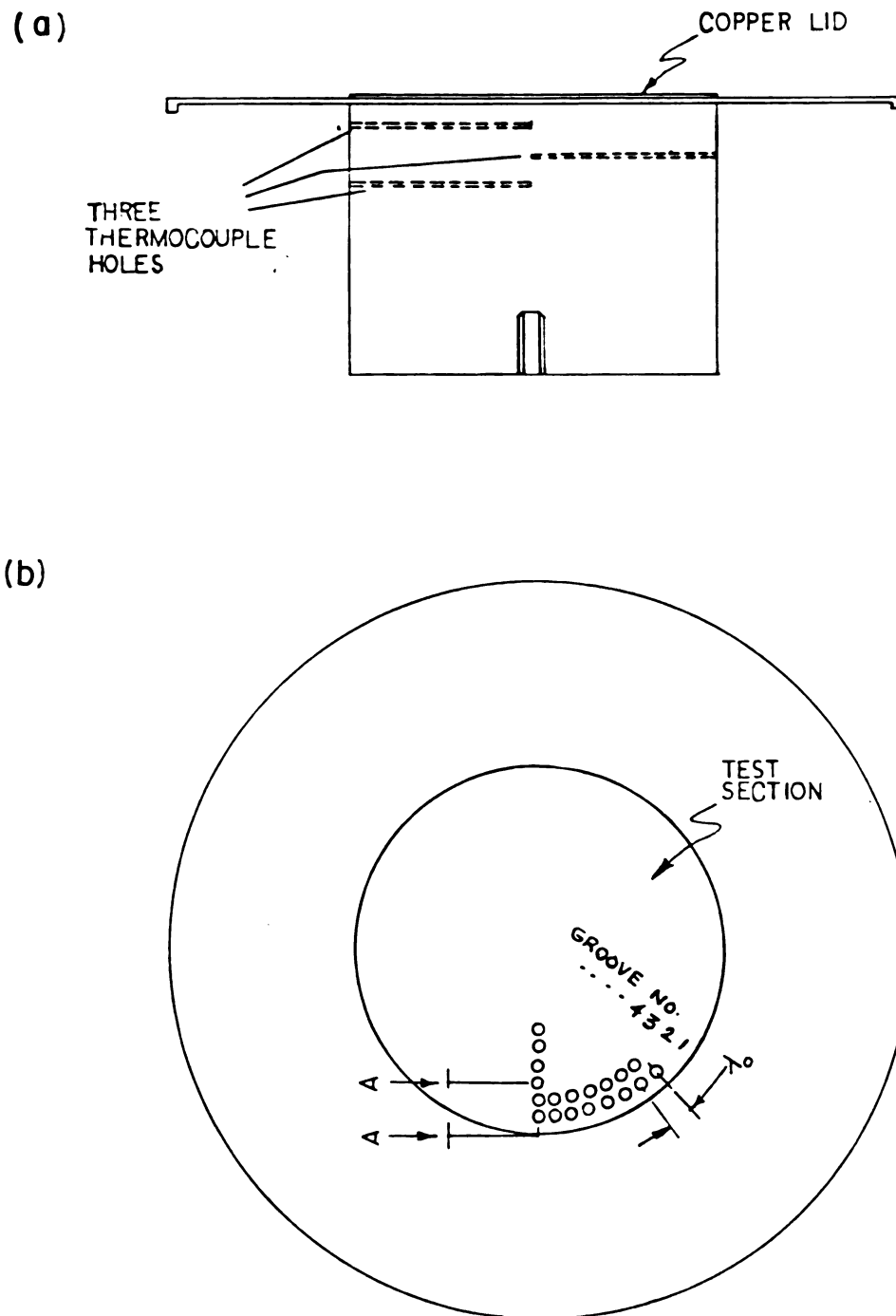
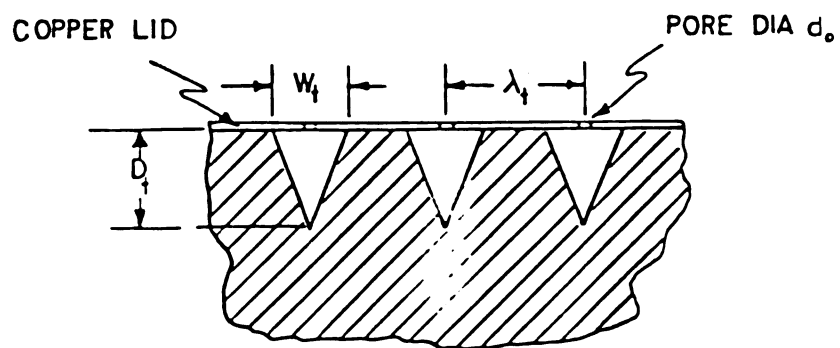


Figure 17. Test surface; (a) Side View
(b) Top View

(c)

SECTION A-A

(d)

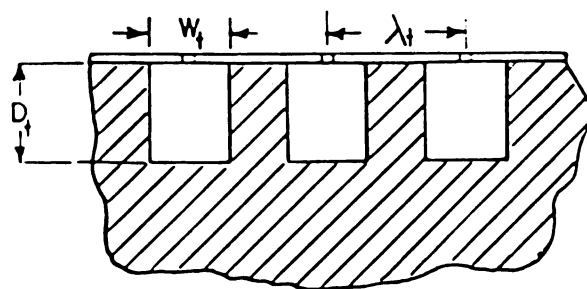


Figure 17 (continued) (c) and (d) Groove cross-sections.

Table 2. Structural dimensions of the test surfaces					
Surface No.	d_o	λ_o	λ_t	D_t	w_t
1	0.18	0.60	0.60	0.50	0.25
2	0.25	0.60	1.20	0.50	0.25

(mm)

loss in the radial direction. A high temperature resistant and low thermal conductivity adhesive was used to stick a circular ring at the bottom of the thin section of the test surface. The ring is in turn screwed to a cylindrical shell. Figure 18 shows the pool boiling setup.

A specially designed nichrome filament heater is tightly screwed to the bottom of the test surface and is used to heat the test section. The assembly is then sealed off with a flanged U-tube. The heater supply and thermocouple wires run through the U-tube and out to the instrumentation panel. The whole assembly is then immersed in a large beaker containing double distilled water, maintained at saturation temperature through direct heating from a hot plate. Another smooth (ordinary machined) brass surface was also manufactured and tested to compare the enhancement effect of the special surfaces.

An adjustable D.C. power supply, monitored by a digital multimeter (DMM) was used for the test section heater.

Figure 19 shows the power supply circuit. Copper-constantan thermocouples and a digital thermometer were used to measure temperatures. Three thermocouples under the test section were used to record the temperature at distances of 2, 4 and 6mm from the top of the surface. Another thermocouple was used to record the bulk liquid temperature.

The beaker and the test section were cleaned with acetone before each test. The water level in the beaker was maintained about 10cm above the test section by periodic replenishment during the test while the pool of water was maintained at saturation temperature by a hot plate. The maximum subcooling noted was 0.3°C . The test section heater power supply was increased slowly in steps and then decreased following the same steps.

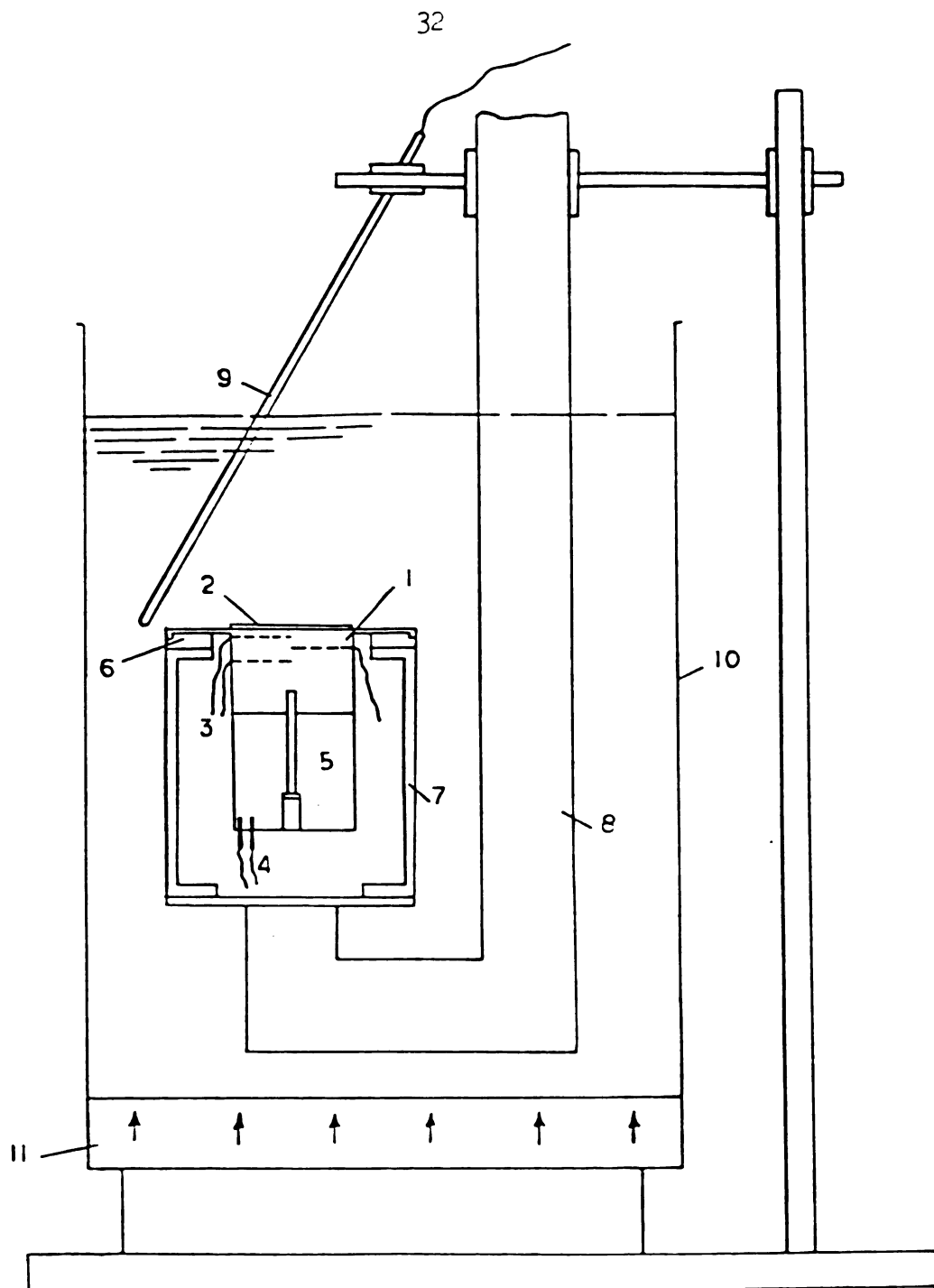


Figure 18: U-tube pool boiling facility (legend: 1- test section, 2. test surface 3. thermocouple wires, 4. power leads 5. heater, 6. circular ring attached to the test surface using low conductivity adhesive, 7. cylindrical shell, 8. flanged U-tube, 9. thermometer for measuring bulk temperature, 10. beaker, 11. hot plate).

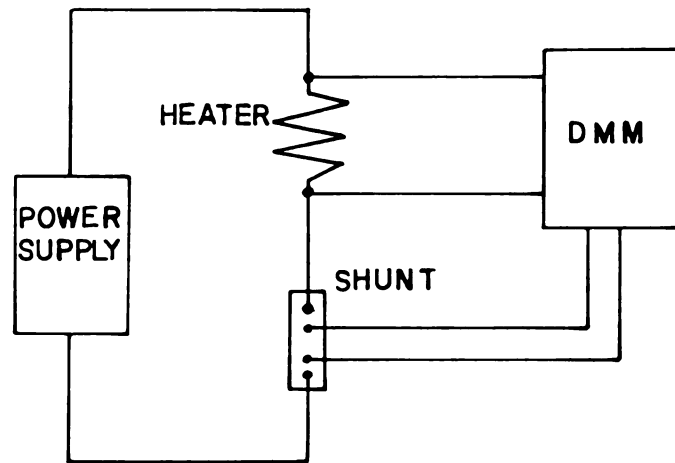


Figure 19. Power Supply Circuit.

The following readings were taken after steady state conditions were reached at each step:

1. Temperature at 2mm (from the top of the surface), T_2
2. Temperature at 4mm (from the top of the surface), T_4
3. Temperature at 6mm (from the top of the surface), T_6
4. Voltage drop across test section heater, V_H with the DMM
5. Voltage drop across the shunt, V_S with the DMM.
6. Bulk water temperature, T_{sat}

The following calculations are performed to find the heat transfer coefficient, h .

The electrical current, I , flowing through the circuit is obtained from

$$I = \frac{V_S}{R_S} \quad (3-1)$$

where R_S is a known shunt resistance and V_S is the voltage drop across the shunt measured with the DMM.

The power input to the heater is calculated as

$$\text{Power} = V_H I \quad (3-2)$$

and then the heat flux, q , is determined from:

$$q = \text{Power}/A_S \quad (3-3)$$

where A_S is the projected surface area of the test section.

The wall temperature, T_w , is obtained from

$$T_w = T_2 - (T_4 - T_2) \quad (3-4)$$

The wall superheat then is

$$\Delta T = T_w - T_{\text{sat}} \quad (3-5)$$

and the heat transfer coefficient is calculated from

$$h = q/\Delta T \quad (3-6)$$

It is assumed in the above calculations that all the input heat flows through the test section i.e., negligible radial heat conduction to the outer section of the surface and negligible radiation and natural convection losses inside the cylindrical shell. Also, assuming a linear temperature gradient, the temperatures at 2 and 4mm are used to extrapolate to the surface temperature, T_w . The data recorded and listed in appendix A show that the temperature gradient between 6, 4 and 2mm from the surface is very close to being linear at lower heat fluxes. At higher heat fluxes it is somewhat off because of possible radiation and natural convection losses inside the cylindrical shell and radial conduction losses to the outer section of the test surface. Total heat losses were estimated to be about 5%. Appendix B gives a discussion of the experimental errors involved in the measurements.

3.2 Visualization experimental design and procedures

The apparatus was designed to visualize the evaporation phenomenon in the grooves. The observation was along the axis of the groove rather than from the side as in Nakayama's case. Also, the apparatus was designed with grooves made with brass walls to exactly simulate the grooves on the actual test surface while in the Nakayama study the continuous grooves had glass walls.

The apparatus, shown in Figure 20, consists of a base block made from brass with grooves machined across the axis of the base block. The grooves are covered with a copper lid (shim stock) containing micro-drilled holes, and two thin glass plates (24mm x 30mm) forming a pool space above the base block. These components are pasted together carefully with a high temperature resistant epoxy so that no microscopic paths for the fluid existed between the tunnels and the pool other than the holes (pores) in the lid. The pore sizes used were 0.15mm and 0.25mm. There were three pores on top of each groove.

The pool was filled with double distilled water, its top open to atmosphere. Water was replenished with a dropper during the experiment. Heat was supplied through a D.C. power controlled heater under the base block. The evaporation process in the grooves of three different cross-sectional geometries (triangular, rectangular and circular) was recorded using a videotape camera and recorder and a motor driven still camera. The groove size was also varied to study the effect of change in size on the evaporation process inside the grooves.

Heat transfer measurements could not be made with the visualization test section because of high heat losses to the environment from the base plate and the glass walls.

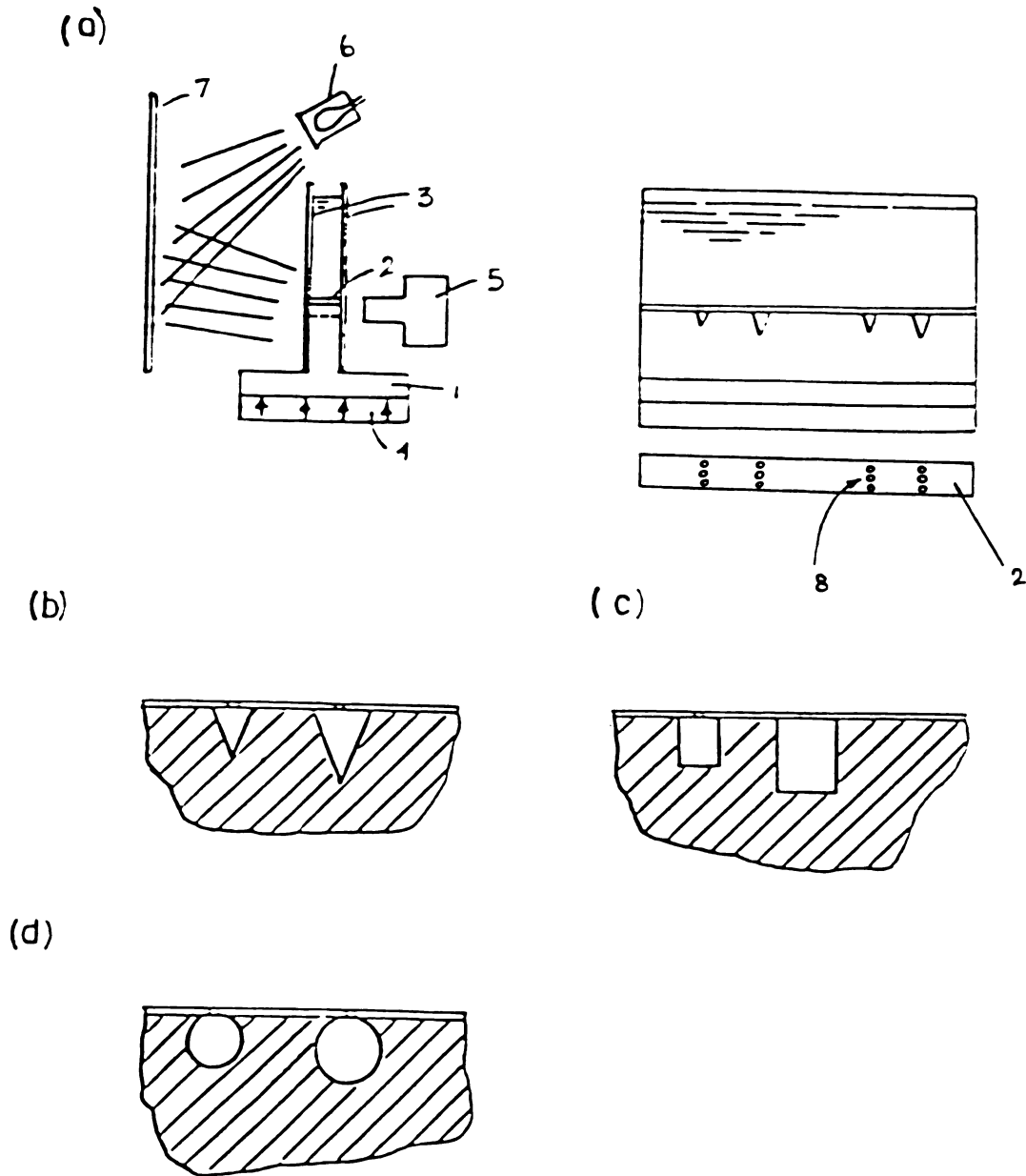


Figure 20. Visualization experimental setup. (a) schematic diagram (Legend: 1. brass base block, 2. copper lid, 3. glass plates, 4. heater, 5. camera, 6. florescent light, 7. diffusely reflecting screen, 8. pores); (b) triangular grooves cross-section; (c) rectangular grooves cross-section; (d) circular grooves cross-section.

4.0 RESULTS AND DISCUSSION

4.1 Pool boiling curves

The data recorded from the pool boiling tests is included in the appendix A. Separate curves for each experimental run are plotted in Figures 21 through 26. The data averaged over two experiments on each surface is plotted in Figure 27 along with two curves for the Nakayama enhanced surfaces (coded surfaces No. 3 and No. 4). Also, the smooth surface pool boiling curve obtained by Nakayama is shown.

As shown in Figure 27, surface No. 1 performs well at low heat fluxes but reverts towards the smooth surface behavior at intermediate heat fluxes. Surface No. 2 is better over a higher range of heat flux and shows about a seven-fold improvement in the boiling heat transfer coefficient over the smooth surface of Nakayama.

Nakayama and coworkers performed their tests over a relatively high heat flux range. Their curves show an improved behavior as the pore diameter is decreased approximately to the range of 0.1-0.25mm. However, the present surface No. 2 (pore dia. 0.25mm) did behave better than Nakayama's surface No. 3 (pore dia. 0.2mm) at least over the available common part of the heat flux range. It is also interesting to note that the tunnel pitch, λ_t , in the present surface No. 2 was 1.2mm compared to 0.6mm in the Nakayama's surface No. 3. This means that the groove spacing is rather a flexible dimension (within a certain range) and as long as a continuous supply of liquid enters through the pores and subsequent (thin film) evaporation in the grooves is assured the surface will give good results.

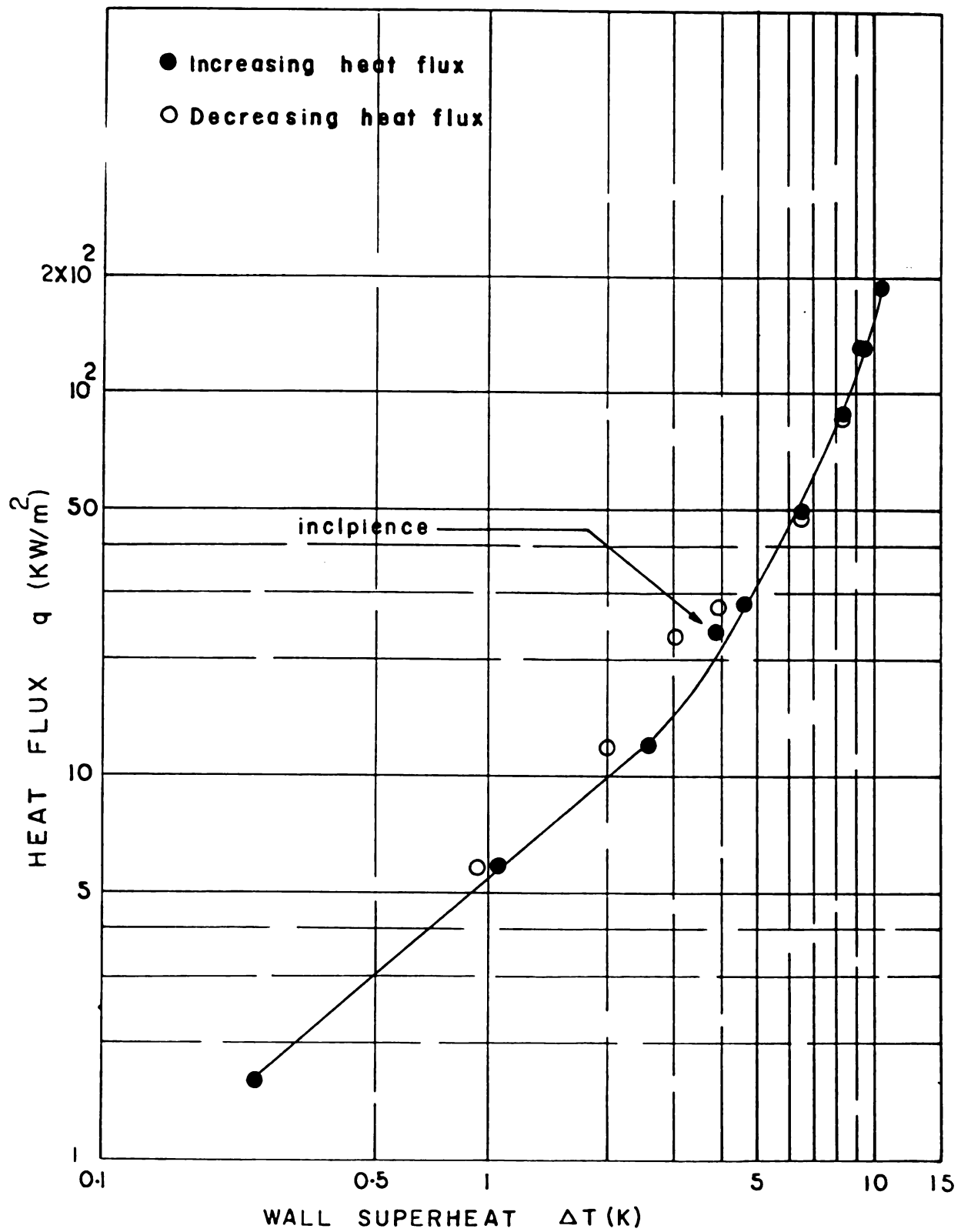


Figure 21. First pool boiling curve for the smooth surface.

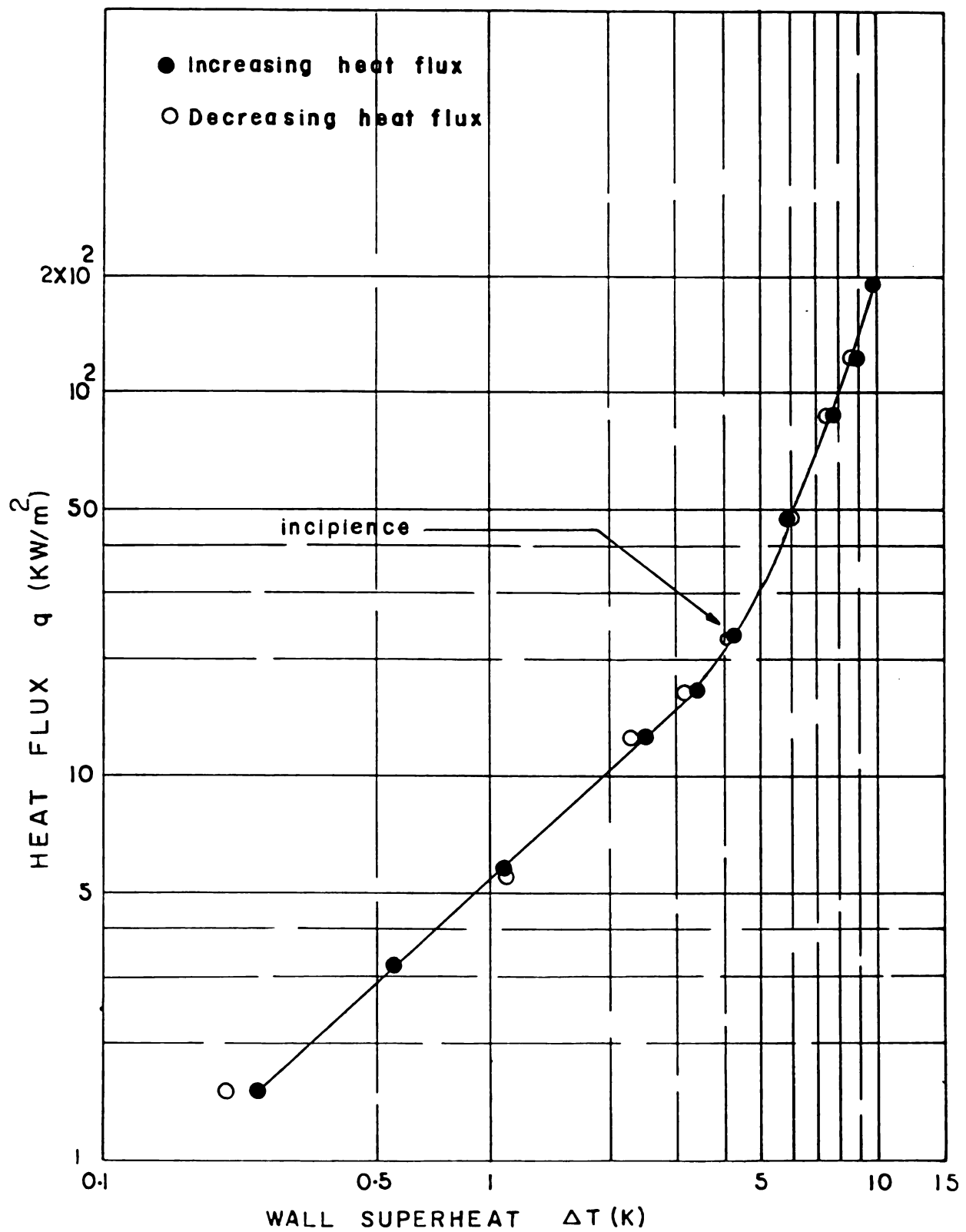


Figure 22. Second pool boiling curve for smooth surface.

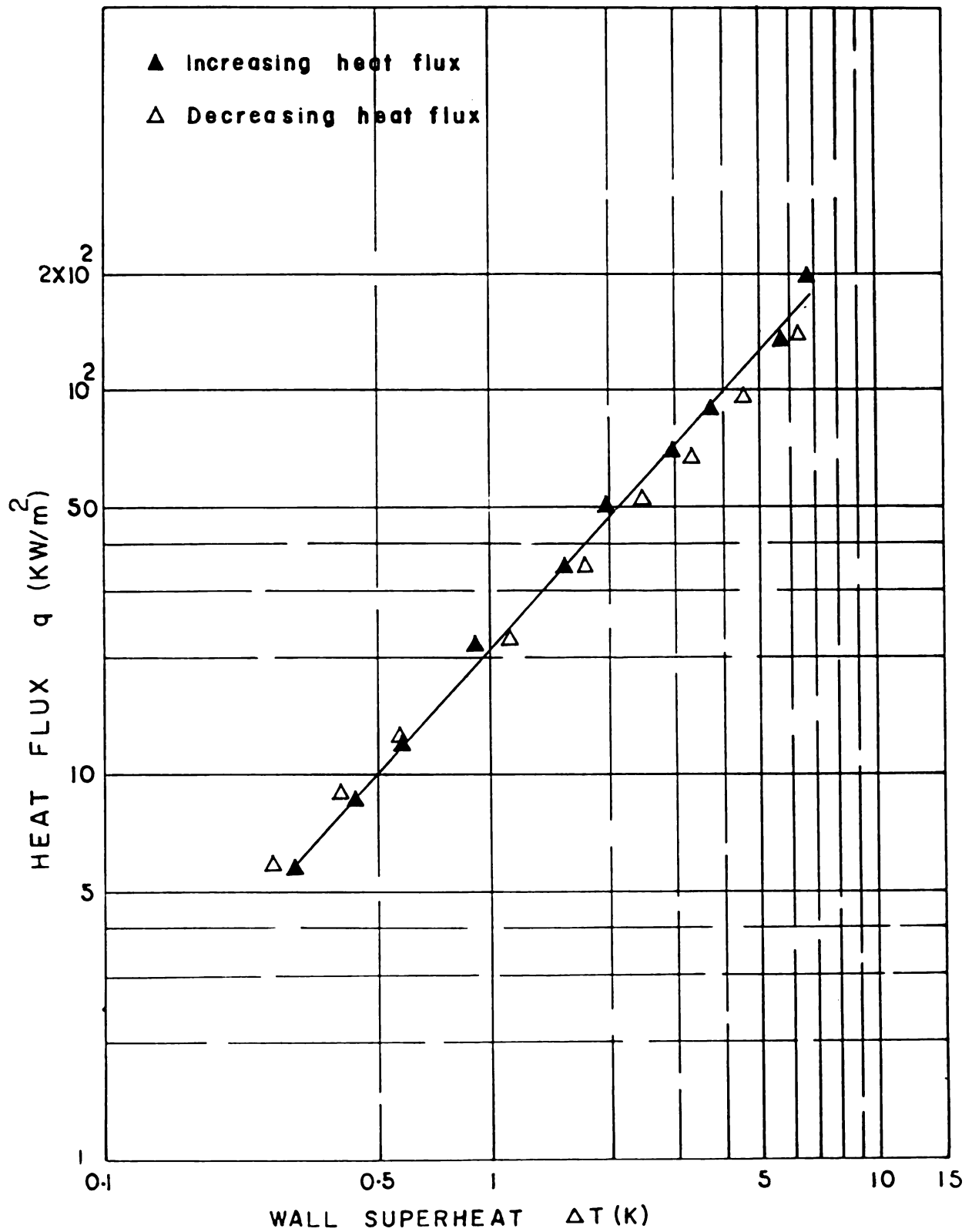


Figure 23. First pool boiling curve for Surface No. 1.

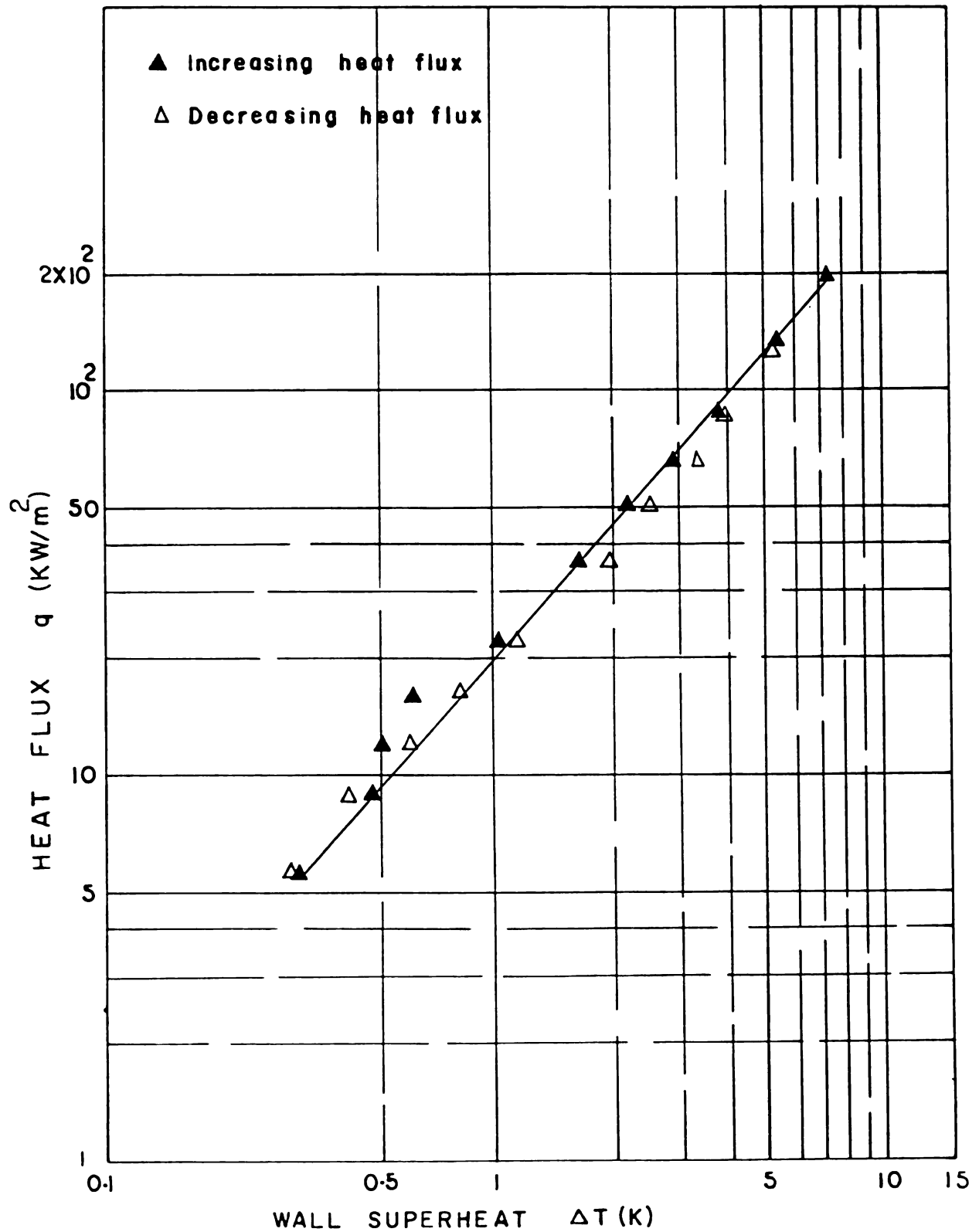


Figure 24. Second pool boiling curve for Surface No. 1.

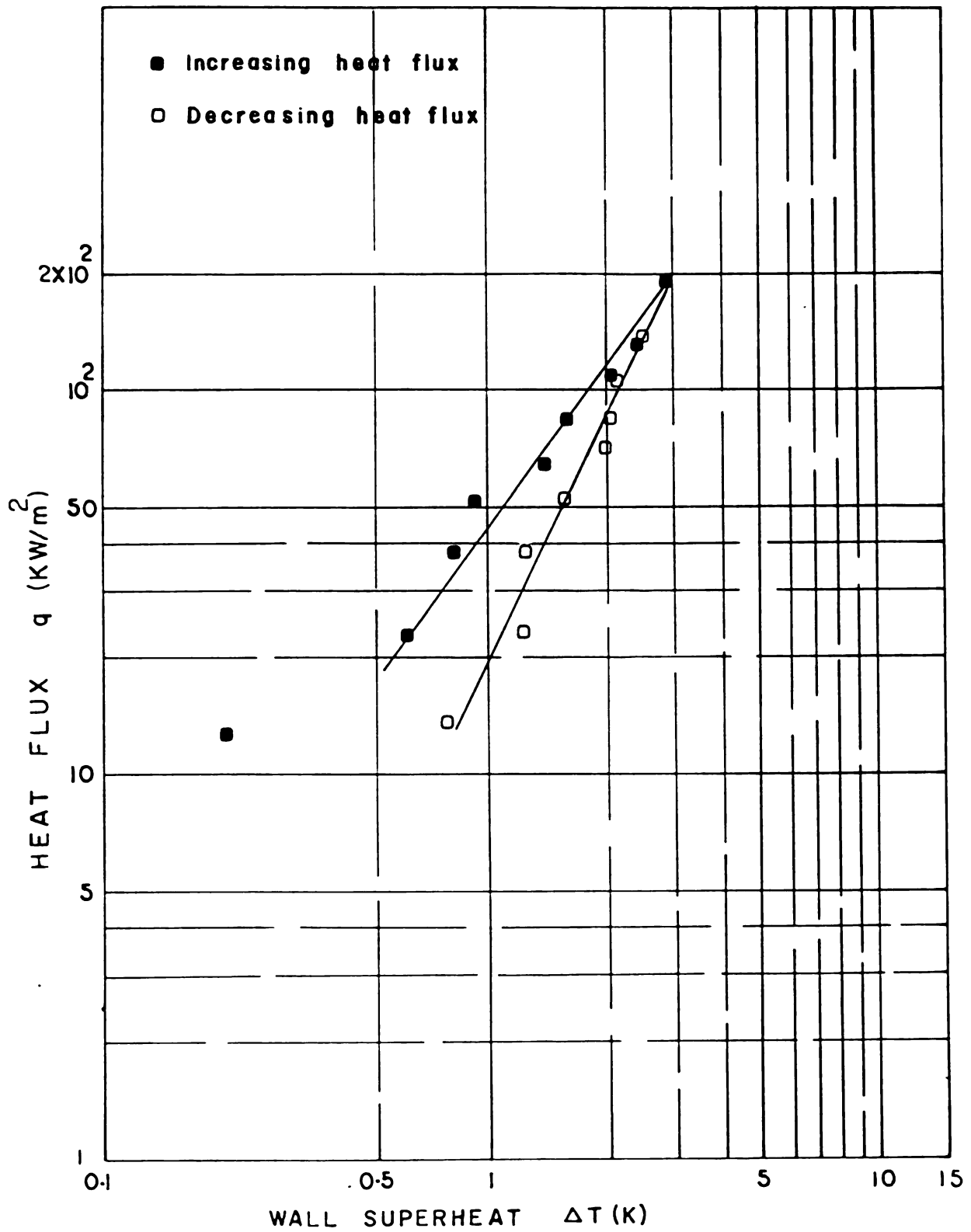


Figure 25. First pool boiling curve for Surface No. 2.

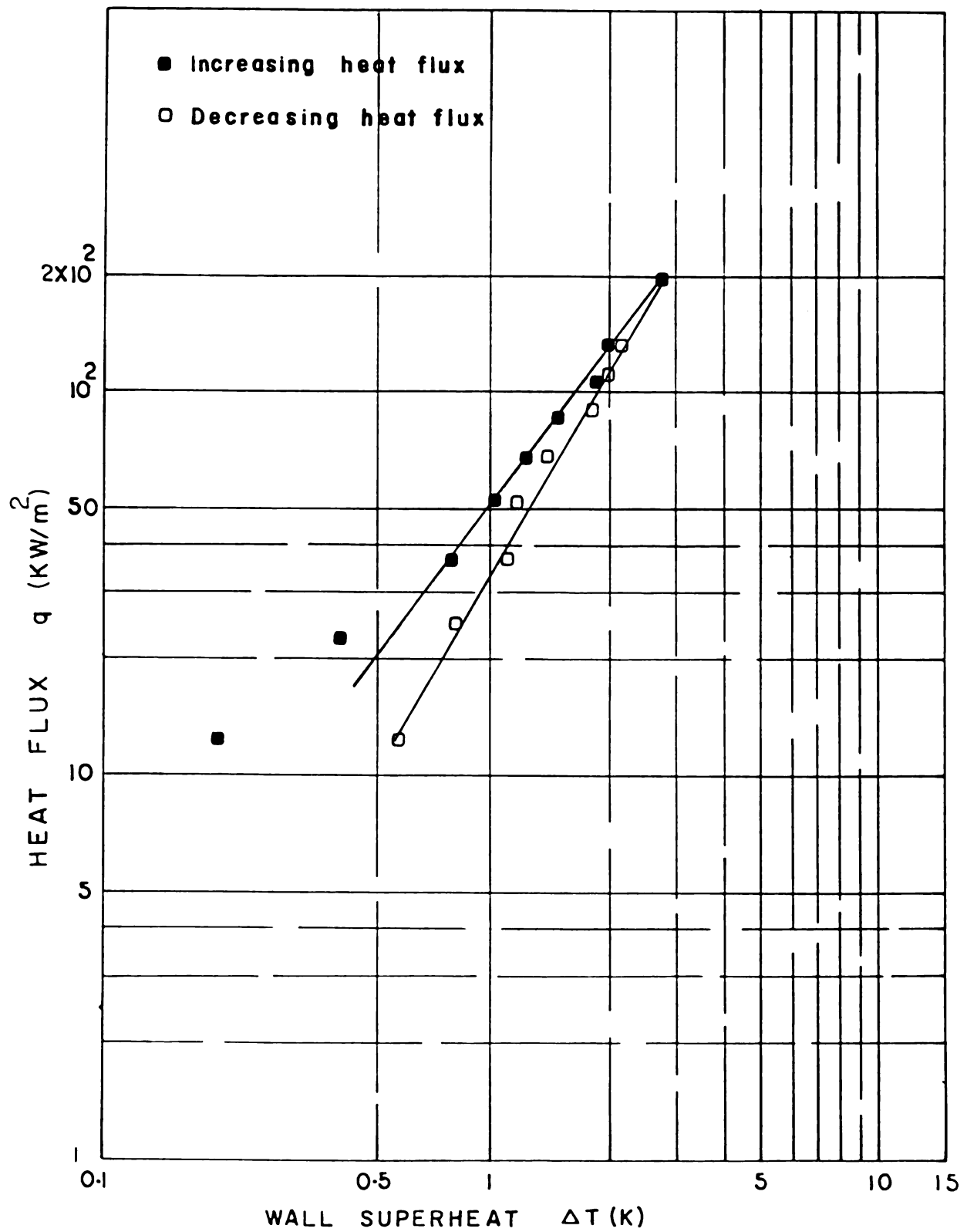


Figure 26. Second pool boiling curve for Surface No. 2.

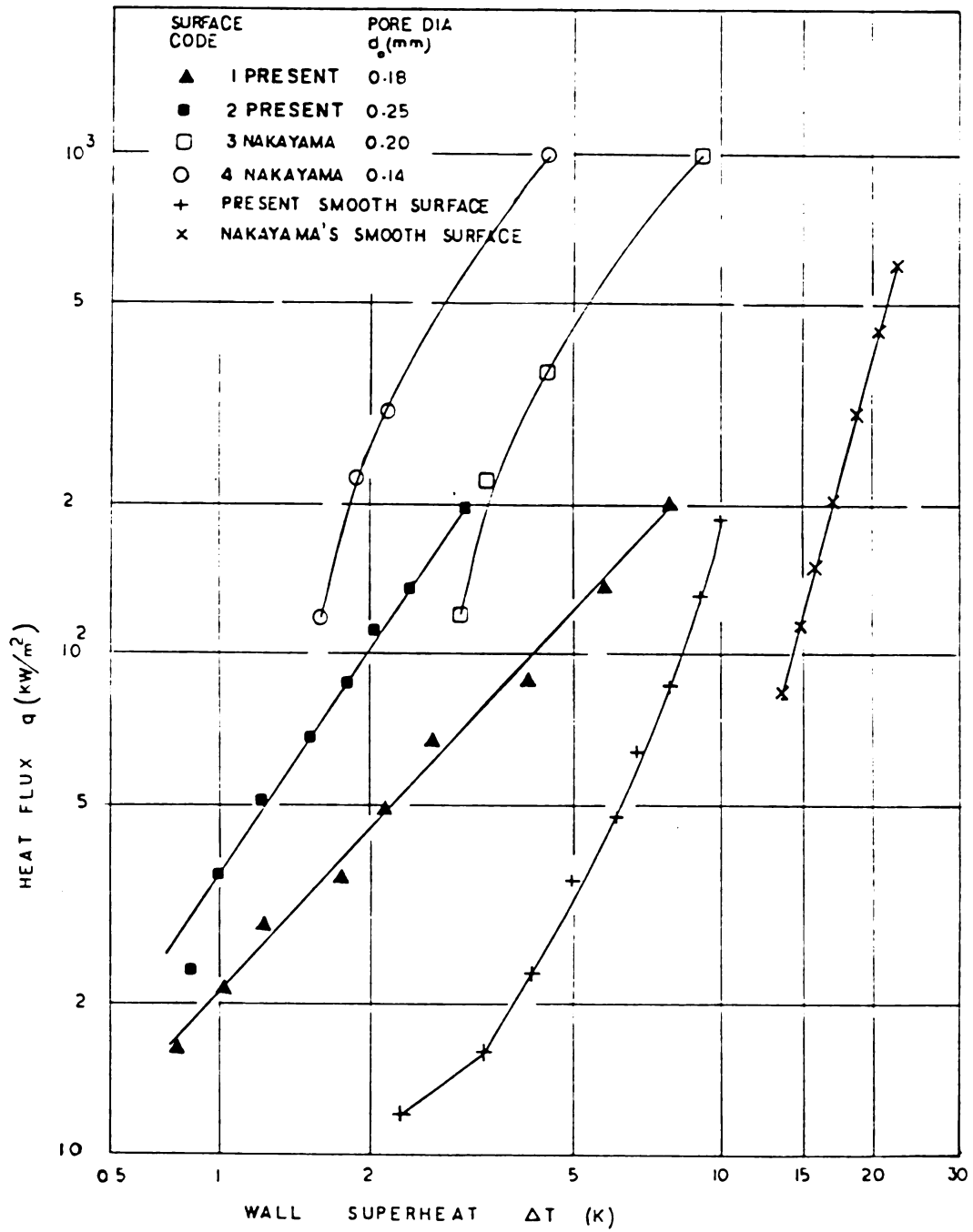


Figure 27. Pool boiling curves.

There was no appreciable boiling curve hysteresis for the present surfaces (see Figures 23-26 where data is plotted both while increasing and decreasing the heat flux). Bergles and Chyu [15], however, reported substantial hysteresis for the HIGH FLUX surface where a wall superheat of 8°C was reached before there was an explosive formation of vapor and a reduction in the wall superheat to about 0.5°C . Such temperature overshoot presents potential startup problems.

The present surface No. 1 and No. 2 behave slightly better in terms of the heat transfer coefficient while increasing the heat flux than while decreasing it. This behavior was consistent in all the experiments (see Figure 23-26), however, it is more obvious for surface No. 2.

It should be noted that a wall superheat of about 4°C was required for incipience on the smooth surface (see Figure 27) while the activation of enhanced surfaces No. 1 and No. 2 was almost immediate at applying a minimum level of heat flux (about 0.4 kW/m^2). The wall superheat, ΔT , was observed to be 0.1°C or less at this heat flux.

An appreciable difference in the performance of the present smooth surface and that of Nakayama's could be accounted for by one's definition of a smooth surface. The present smooth surface was an ordinary machined brass surface. A highly polished surface not permitting efficient nucleate boiling could behave far worse than a machined surface. Thus the datum for comparing the enhanced surfaces is not fixed. In reality, the datum should be an ordinary surface as used in industrial practice.

4.2 Visualization of the evaporation phenomenon inside the grooves

The events summarized below were commonly observed in the visualization experiments.

In an unheated state a vapor region existed in the corners of the grooves; this was confirmed by observing the evaporation phenomenon starting usually from one of these corners each time heat was applied. In the case of circular cross-section grooves, evaporation started from different spots along the periphery. A typical schematic of the activation of a groove is shown in Figure 28. As soon as the vapor-liquid interface hit the pores, vapor started coming out of one of these pores in the form of bubbles. At this instant the liquid in the groove would form a film on the groove walls with most of the liquid held in the corners by surface tension forces. Thereon the liquid entered intermittently through the inactive pore which was indicated by the pulsation of the liquid-vapor interface in the groove. In all three geometries tested (triangular, rectangular and circular) evaporation of a thin liquid film was consistently observed. Figure 29 shows schematics of the shapes of the film in these three geometries.

Circular grooves generally required a larger superheat to become active and could become flooded at low heat flux. At intermediate heat fluxes a uniform thin film spreading along the periphery was observed. Triangular grooves behaved well at low heat fluxes but at intermediate heat fluxes the bottom corner seemed to dryout. This explained the movement of the boiling curve of surface No. 1 towards the smooth surface curve at intermediate heat flux levels (see Figure 27). However for a larger pore size (0.25mm) similar grooves did show a stable thin film evaporation at intermediate heat fluxes. At higher heat fluxes the liquid menisci become less and less apparant in all the three geometries.

A combination of two different pore diameters on the same groove showed that the larger pore remained inactive, perhaps serving to pump

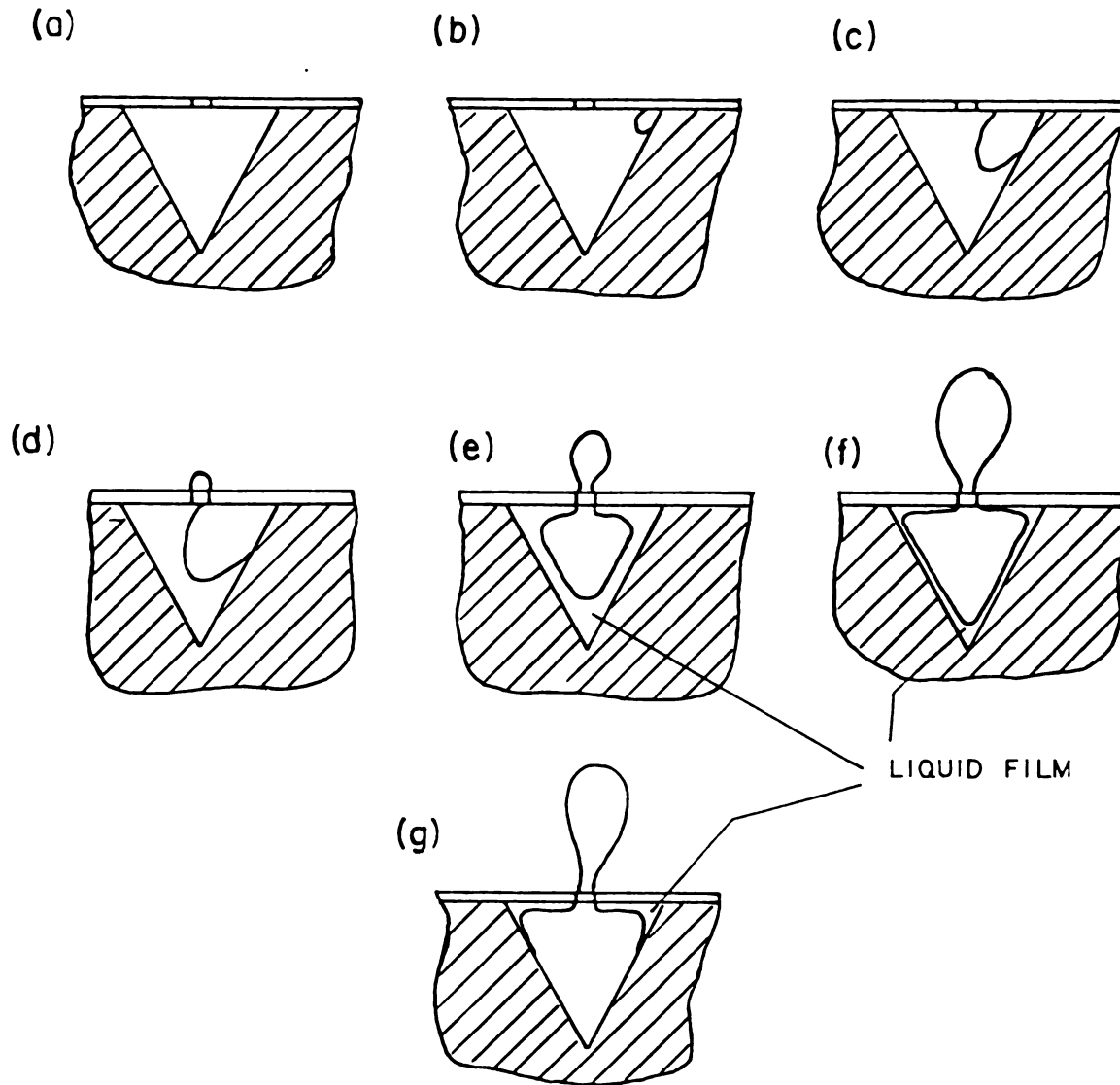


Figure 28. Schematic sequence of activation of a vapor pocket and film dryout at medium heat flux.

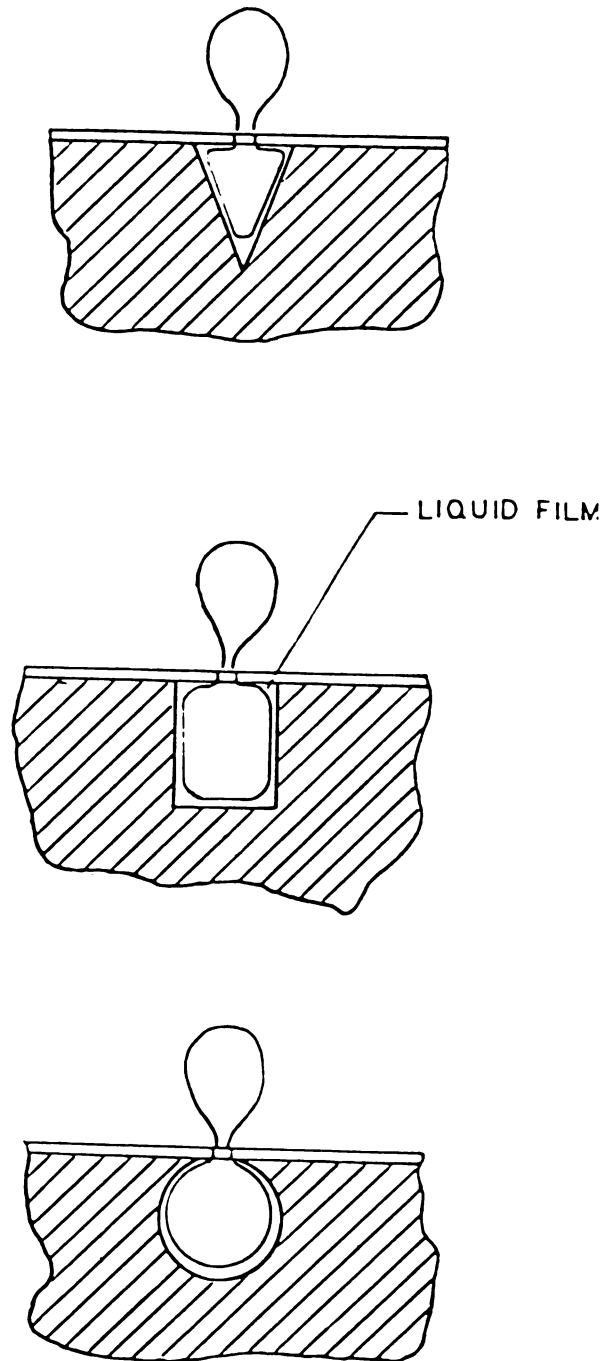


Figure 29. Schematic of shape of film in three geometries.

water into the groove while the smaller size pores acted as boiling sites. The grooves with depths greater than the order of 1mm remained mostly flooded (perhaps due to the domination of gravitational forces over the capillary and surface tension forces). However, as the heat flux is increased they behave better.

A number of photographs taken during the experiments using a motor-driven still camera are included here in an effort to explain some of the events summarized above. The magnification on these photographs is approximately 20 times the original size of the grooves. The groove depth was approximately in the range of 0.75-1.2mm. These photographs have been numbered as Figures 31 through 61. Grooves are coded for identification as follows:

- T1 : Triangular groove No. 1 (pore dia 0.17mm)
- T2 : Triangular groove No. 2 (pore dia 0.17 and 0.25mm)
- R1 : Rectangular groove No. 1 (pore dia 0.25mm)
- C1 : Circular groove No. 1 (pore dia 0.17 and 0.25mm)
- C2 : Circular groove No. 2 (pore dia 0.17 and 0.25mm)

Figures 30 through 35 show a typical sequence of activation of the groove T1. At low heat flux liquid is held in the corners (see Figure 33) but as the heat flux is increased the liquid film is not apparant. In fact, the lower portion of the groove seems to have dried out (compare Figure 34 to Figure 35). Figures 36 and 37 show the groove flooding as the heating is stopped.

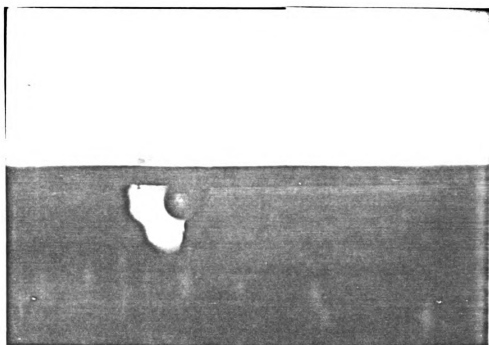


Figure 30. (T1) Evaporation starts from right corner.

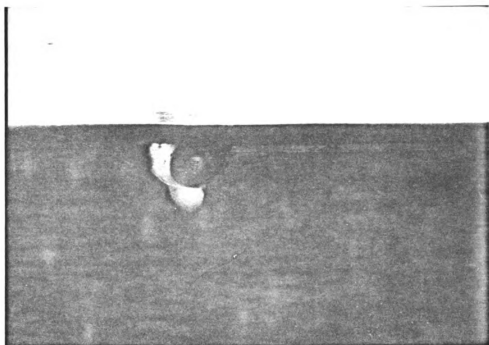


Figure 31. (T1) Vapor front advancing in the groove.

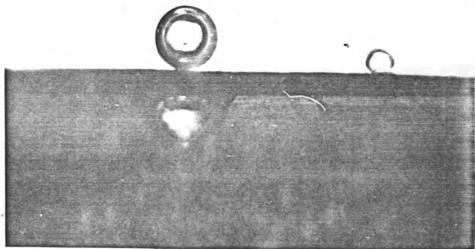


Figure 32. (T1) Vapor starts coming out of the groove, liquid inside forms of a film on the groove walls.

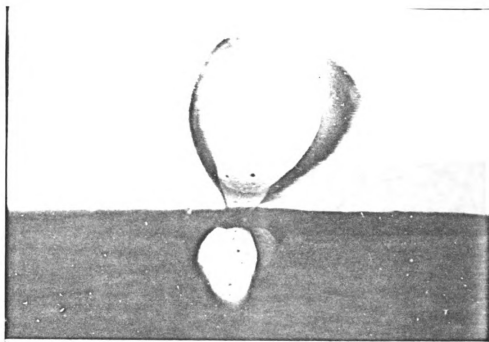


Figure 33. (T1) At low heat flux liquid film is apparent.

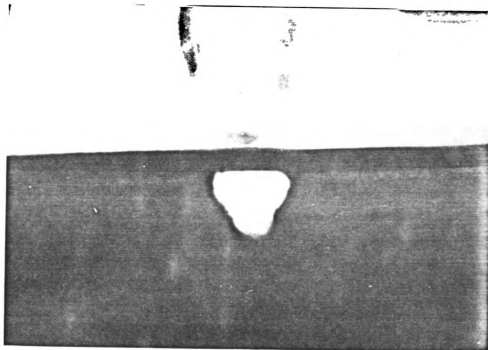


Figure 34. (T1) At intermediate heat flux lower half of the groove seems to have dried-out (compare with Figure 35).

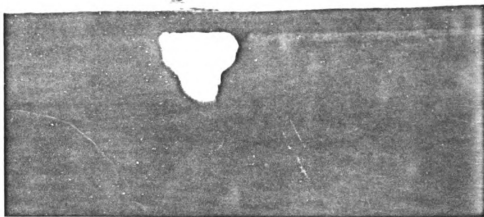


Figure 35. (T1) Flooded groove.

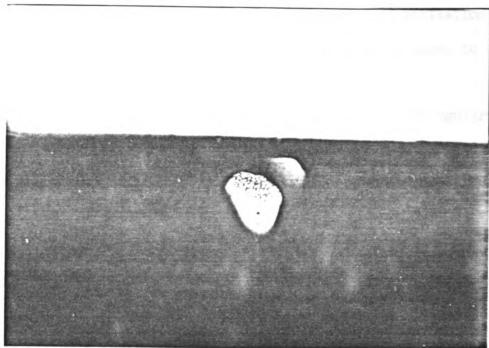


Figure 36. (T1) Liquid-vapor front in the groove as the heating is stopped and groove is getting flooded.

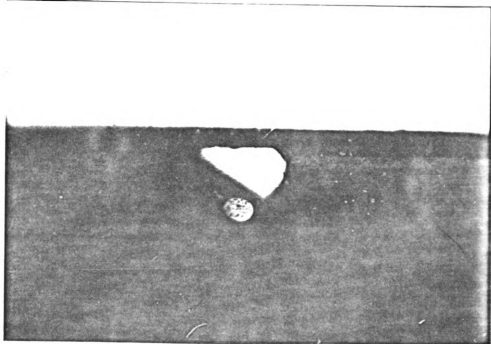


Figure 37. (T1) Groove flooding.

Figures 38 through 43 show another typical sequence of activation of the groove T2. This groove with a larger pore dia (0.25mm) seems to be more stable at intermediate heat fluxes compared to T1.

Figures 44 through 51 show a sequential activation of rectangular groove R1; evaporation starts from the lower right corner, and a liquid film is seen on the groove walls over the lower and intermediate heat fluxes.

However, at higher heat flux the existence of a liquid film is less apparent.

Figures 52 through 55 show the evaporation in circular groove C1. A uniform thin liquid film is seen along the periphery over at low heat fluxes. Figures 56 through 61 show photographs for circular groove C2. Figure 61 shows an interesting view when nucleation is starting from different spots along the periphery at the same time.

4.3 Thin film evaporation

Many researchers have previously argued that the evaporation of a thin film at the base of a growing bubble, microlayer evaporation, is perhaps the most significant mechanism responsible for higher heat transfer coefficients in nucleate boiling. Moore and Mesler [13] showed that 70-90% of the heat flow was accountable to this mechanism in some instances for smooth surfaces.

Based on the fact that this film evaporation was consistently observed in all three geometries studied here and that very high heat transfer coefficients are associated with thin film evaporation, it is concluded that thin film evaporation is the principal heat transfer mechanism in enhanced surface boiling as suggested by several previous investigators. The above conclusion seems particularly true over the low heat flux regime

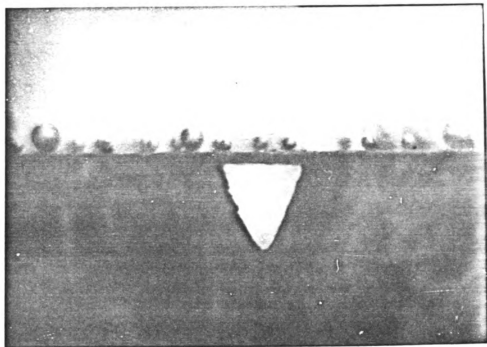


Figure 38. (T2) Flooded groove

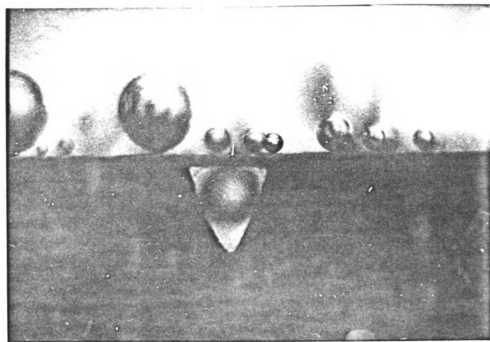


Figure 39. Evaporation starts in the groove.

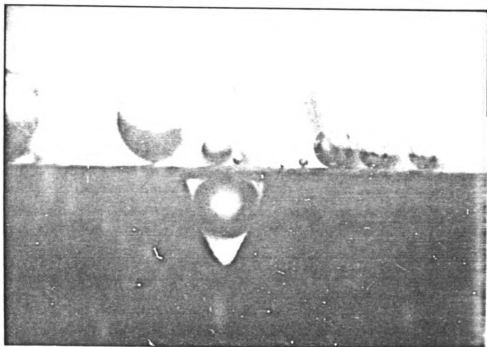


Figure 40. Vapor starting to come out through the pore.

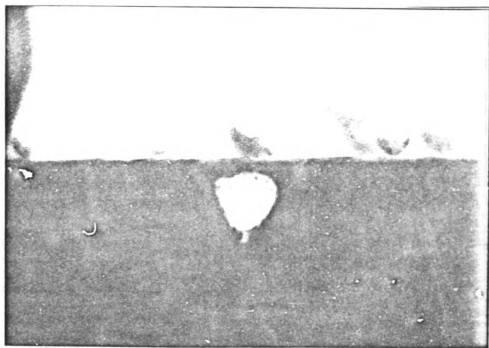


Figure 41. Liquid forms a film on groove walls.

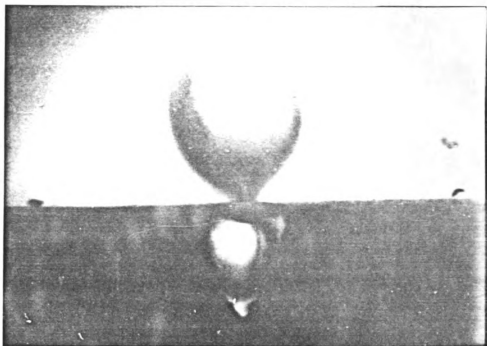


Figure 42. Nucleation at lower heat flux.

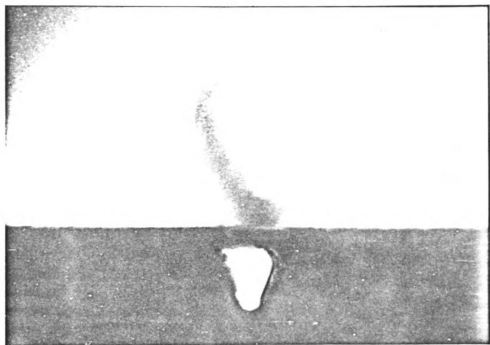


Figure 43. Nucleating groove at intermediate heat flux.

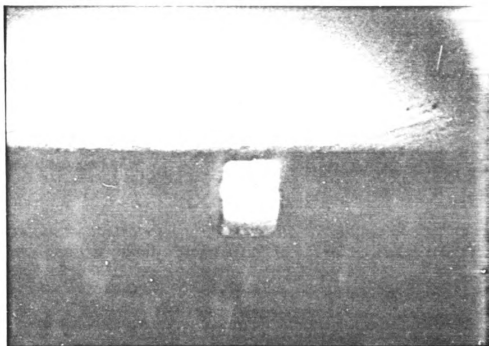


Figure 44. (R1) Flooded groove.

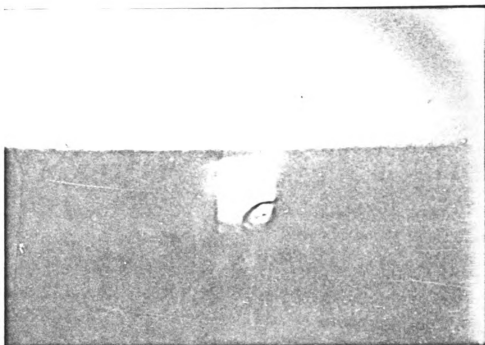


Figure 45. (R1) Evaporation starting from lower right corner.

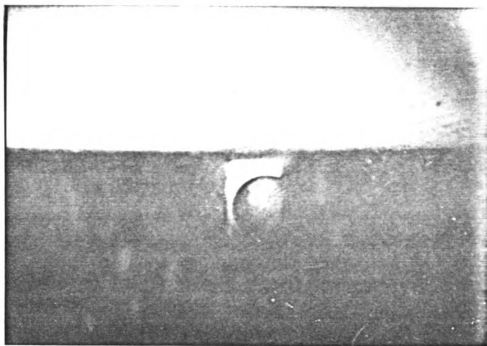


Figure 46. (R1) Vapor front advancing in the groove.

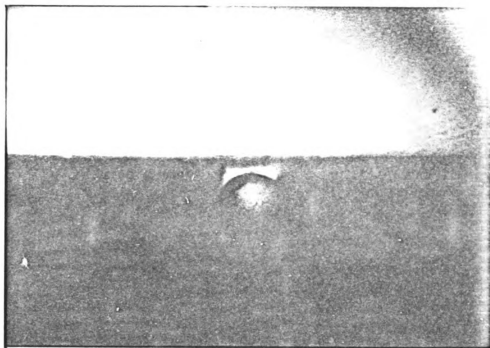


Figure 47. (R1) Liquid being pushed out of the groove.

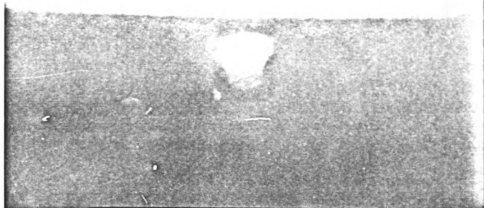


Figure 48. (R1) Nucleating groove at lower heat flux.

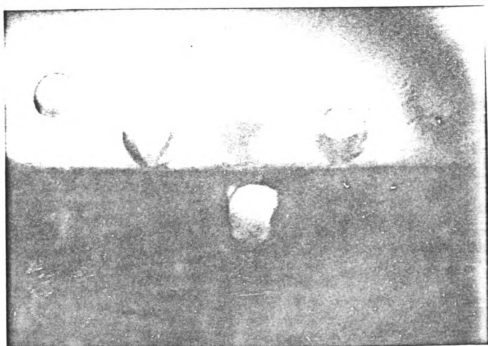


Figure 49. (R1) Nucleating groove at intermediate heat flux.

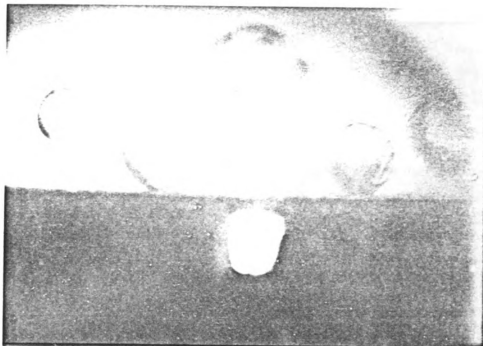


Figure 50. (R1) Nucleating groove at intermediate heat flux.

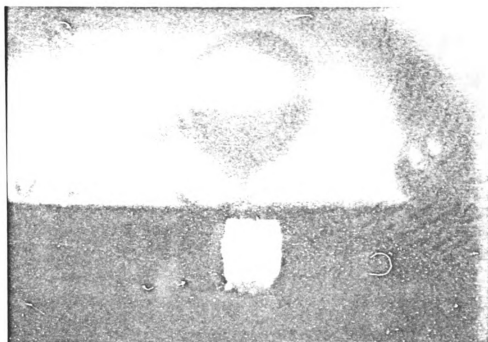


Figure 51. (R1) Nucleating groove (higher heat flux), liquid film is less apparent.

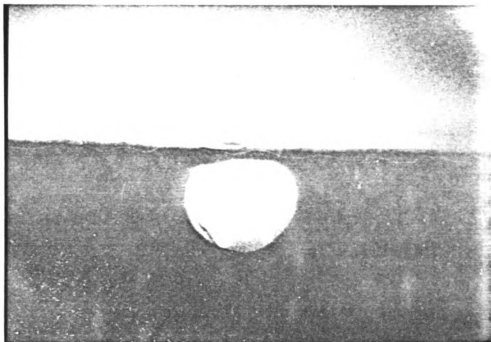


Figure 52. (C1) Flooded groove.

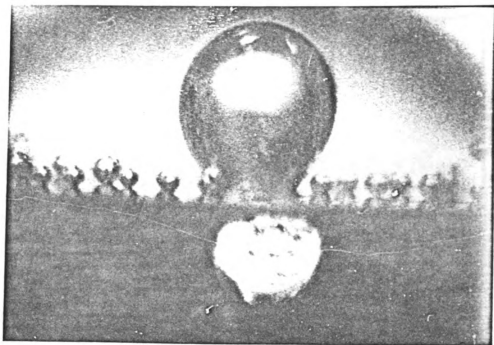


Figure 53. (C1) Nucleating groove (a uniform thin film is seen along the periphery). Low heat flux is applied.

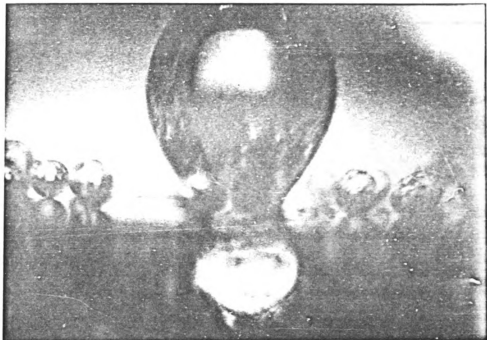


Figure 54. (C1) Nucleating groove (low heat flux).

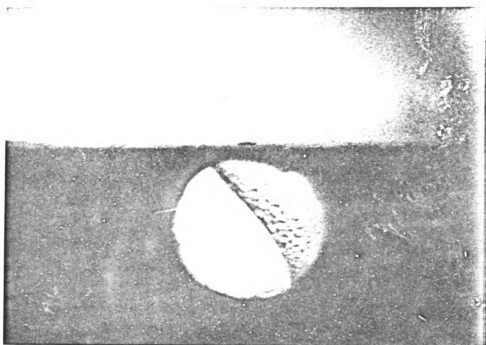


Figure 55. (C1) Groove flooding as the liquid-vapor front moves in when heating is stopped.

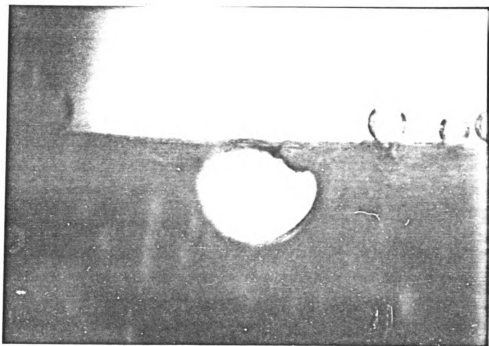


Figure 56. (C2) Flooded groove.

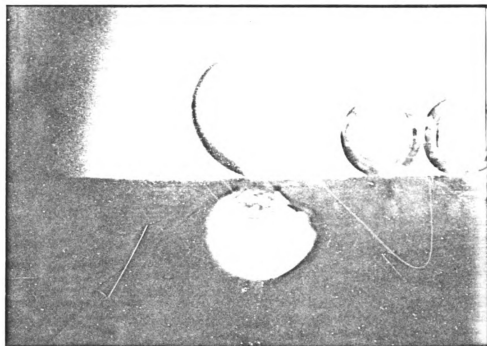


Figure 57. (C2) Nucleating groove.

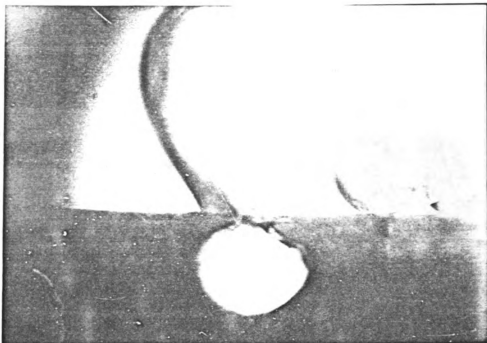


Figure 58. (C2) Nucleating groove (intermediate heat flux).

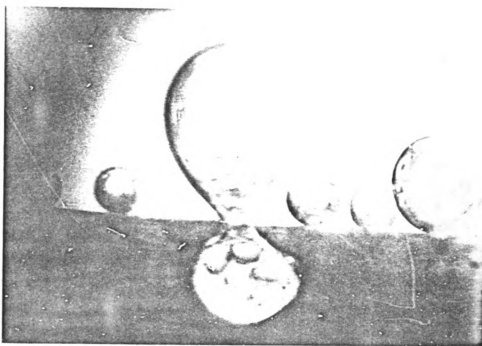


Figure 59. (C2) Nucleating groove (low heat flux). Droplets in groove and bubble are formed by condensation on the glass end plates.

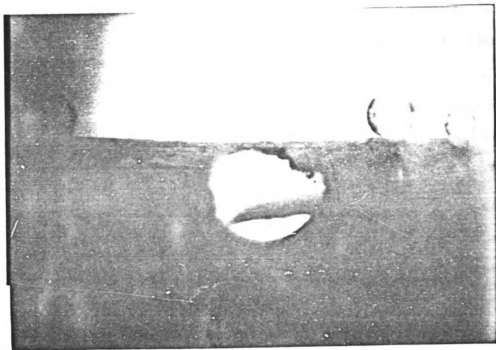


Figure 60. (C2) Groove flooding.

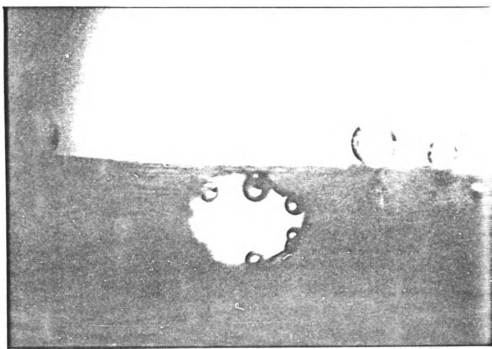


Figure 61. (C2) Evaporation starting at different spots along the periphery.

(up to about 100 kW/m^2) when effectively all the vaporization is taking place inside the structured surface and vapor is being ejected through the pores in the form of bubbles. It is speculated that the actual surface temperature stays very close to the bulk temperature because of the large extraction of heat into the tunnels for thin film evaporation. Therefore, the contribution of natural convection is thought to be negligible.

From the photographs (Figures 31 through 61) the average film thickness is approximated to be of the order of $.02\text{mm}$. The heat transfer coefficient for conduction across the thin liquid film can be obtained by dividing the thermal conductivity of liquid by the film thickness. This will give a heat transfer coefficient of $35 \text{ kW/m}^2\text{-C}$ for thin water film. Therefore we find a good qualitative agreement with the h values obtained for the enhanced surfaces (see appendix A). To get closer agreement a factor greater than one has to be introduced since the effective area covered by the thin film is greater than the projected area of the test surface.

The present study suggests that a mathematical model similar to the one proposed by Gottzmann et. al. [14] based on thin film evaporation could be sought to predict the heat transfer performance of structured surfaces. The most critical factors in this model will be the thickness of the liquid film and the effective area covered by the thin liquid film. For a given surface material and liquid combination, these factors in turn are functions of the geometry of the structured surface, the heat flux and the pore diameter as shown by the visual study. A more sophisticated apparatus could be designed to determine the average film thickness as a function of heat flux for a given groove geometry.

4.4 Comments

The present study also shows that the structured surfaces with structural dimensions of the order of 1mm could still be effective in terms of enhancement. Such dimensions are easily obtainable in cold metal working in order to manufacture these surfaces more economically. Also these do not seem to present any startup problems as long as the internal structure is carefully designed to ensure vapor trapping.

Since the enhanced boiling surfaces have application to multicomponent boiling in the chemical processing and refrigeration industries, their performance in this regard is very important. Thome [19], based on some of his most recent work [20] and the assumption that the bulk saturated binary liquid entering the porous matrix is completely evaporated by thin film evaporation within the matrix such that the only saturated vapor exits, has shown that only a minor improvement in the boiling heat transfer coefficient at the more volatile mixture compositions can be expected. He has strongly recommended experimental research to test this conclusion.

5.0 CONCLUSIONS

The following conclusions are made concerning nucleate pool boiling on enhanced surfaces based on the present study.

1. Thin film evaporation is the principal heat transport mechanism.
2. The geometrical shape of the grooves used to produce an enhanced surface of the type tested here affects the shape and formation of the thin evaporating liquid film.
3. Dryout of the liquid film causes the surface to revert to the performance of a smooth surface.
4. The pore diameter seems to be the most critical dimension as suggested by many previous investigators. Other structural dimensions are rather flexible within a certain range.

APPENDICES

APPENDIX A

Data for the pool boiling curves

Table 3. Data for the first pool boiling curve for smooth surface (plotted in Figure 21).

T_{sat}	c	T_{10}	T_6	T_2	T_w	$\Delta T = T_w - T_{\text{sat}}$	$n = \frac{c}{\Delta T}$
($^{\circ}\text{C}$)	(kW/m ²)	($^{\circ}\text{C}$)	($^{\circ}\text{C}$)	($^{\circ}\text{C}$)	($^{\circ}\text{C}$)		(kW/m ² - $^{\circ}\text{C}$)
99.9	1.4	100.6	100.5	100.4	100.3	0.3	3.6
99.9	5.4	101.5	101.2	101.1	101.1	1.1	9.1
100.0	12.0	103.5	103.1	102.7	102.5	2.5	4.8
99.9	22.1	105.6	104.8	104.1	103.8	3.9*	5.7
99.9	27.6	106.5	105.3	104.6	104.5	4.6	6.0
99.9	34.3	107.7	106.3	105.4	105.0	5.1	7.6
99.8	48.4	110.0	108.0	106.8	106.2	6.4	7.6
99.7	86.2	114.6	111.1	108.9	107.8	8.1	10.6
99.7	132.1	119.0	113.7	110.6	109.0	9.3	14.2
99.7	189.7	124.4	116.9	112.3	110.0	10.3	18.4
99.7	133.3	119.0	113.7	110.4	108.8	9.2	14.5
99.7	84.8	114.3	110.8	108.7	107.7	8.1	10.5
99.8	48.0	109.9	107.8	106.7	106.2	6.4	7.5
99.8	33.8	107.1	105.7	104.8	104.4	4.6	7.3
99.8	27.5	105.5	104.4	103.8	103.5	3.8	7.2
99.8	22.0	104.4	103.4	102.9	102.7	3.0	7.3
99.8	11.9	102.6	102.1	101.8	101.7	2.0	6.0
99.7	5.4	100.9	100.8	100.7	100.6	0.9	6.0
* incipience							

Table 4. Data for the second pool boiling curve for smooth surface (plotted in Figure 22).

T_{sat} ($^{\circ}\text{C}$)	q (kW/m^2)	T_{10} ($^{\circ}\text{C}$)	T_6 ($^{\circ}\text{C}$)	T_2 ($^{\circ}\text{C}$)	T_w ($^{\circ}\text{C}$)	ΔT $= T_w - T_{\text{sat}}$	$n = \frac{q}{\Delta T}$ ($\text{kW}/\text{m}^2 - ^{\circ}\text{C}$)
100.0	0.4	100.2	100.1	100.1	100.1	0.1	4.0
100.0	1.4	100.5	100.4	100.3	100.25	0.25	5.8
100.0	5.5	101.3	101.2	101.1	101.1	1.1	5.0
100.0	12.1	103.8	103.2	102.7	102.5	2.5	4.8
100.0	16.4	105.0	104.4	103.8	103.4	3.5	4.7
100.0	22.3	106.4	105.5	104.6	104.2	4.2*	5.3
99.9	48.8	110.1	108.1	106.6	105.9	6.0	8.1
99.9	86.6	114.3	110.7	108.4	107.3	7.4	11.7
99.9	132.1	118.7	113.3	110.0	108.4	8.5	15.5
99.9	190.3	124.2	116.5	111.8	109.5	9.6	19.8
99.9	132.7	118.9	113.4	110.0	108.3	8.4	15.8
100.0	85.8	114.2	110.7	108.4	107.3	7.3	11.7
100.0	47.0	110.1	108.2	106.8	106.1	6.1	7.7
100.0	21.0	106.2	105.3	104.4	104.0	4.0	5.3
100.0	16.0	104.8	104.0	103.4	103.1	3.1	5.2
100.1	11.9	103.5	103.0	102.6	102.4	2.3	5.2
100.1	5.4	101.6	101.4	101.2	101.1	1.1	4.9
100.2	1.4	100.5	100.5	100.4	100.4	0.2	7.1

*incipience

Table 5. Data for the first pool boiling curve for enhanced Surface No.1 (plotted in Figure 23).

T_{sat} ($^{\circ}\text{C}$)	q (kW/m^2)	T_{10} ($^{\circ}\text{C}$)	T_6 ($^{\circ}\text{C}$)	T_2 ($^{\circ}\text{C}$)	T_w ($^{\circ}\text{C}$)	$\Delta T = T_w - T_{\text{sat}}$	$n = \frac{q}{\Delta T}$ ($\text{kW/m}^2 - ^{\circ}\text{C}$)
100.0	5.3	100.8	100.6	100.4	100.3	0.3	17.7
99.9	8.4	101.0	100.7	100.5	100.3	0.4	19.2
99.9	12.0	101.4	101.0	100.7	100.5	0.6	20.1
99.9	21.6	102.4	101.7	101.2	100.8	0.9	24.0
100.0	34.2	103.8	102.7	102.0	101.5	1.5	22.8
100.0	48.6	105.3	103.8	102.8	102.0	2.0	24.3
100.0	67.6	107.4	105.3	104.0	103.0	3.0	22.5
100.0	85.5	109.4	106.8	105.1	103.8	3.8	22.5
99.9	133.8	115.2	111.1	108.0	105.6	5.7	23.5
99.8	195.5	122.2	116.5	110.9	106.5	6.7	29.2
99.9	138.6	116.0	111.9	108.6	106.0	6.1	22.7
99.9	88.3	110.2	107.4	105.6	104.3	4.4	20.1
99.9	65.1	107.5	105.5	104.2	103.2	3.3	19.7
99.9	49.3	105.7	104.2	103.2	102.4	2.4	20.5
100.0	34.0	104.0	102.8	102.2	101.7	1.7	20.0
100.0	22.3	102.6	101.8	101.4	101.1	1.1	20.3
100.0	12.2	101.4	101.0	100.8	100.6	0.6	20.3
100.0	8.5	101.0	100.7	100.5	100.4	0.4	21.3
100.0	5.5	100.8	100.6	100.4	100.2	0.25	22.1

Table 6. Data for the second pool boiling curve for enhanced Surface No. 1 (plotted in Figure 24).

T_{sat} ($^{\circ}\text{C}$)	q (kW/m^2)	T_{10} ($^{\circ}\text{C}$)	T_6 ($^{\circ}\text{C}$)	T_2 ($^{\circ}\text{C}$)	T_w ($^{\circ}\text{C}$)	$\Delta T = T_w - T_{\text{sat}}$	$n = \frac{q}{\Delta T}$ ($\text{kW/m}^2 - ^{\circ}\text{C}$)
100.0	5.5	100.8	100.6	100.4	100.3	0.3	18.3
99.9	8.5	101.0	100.7	100.5	100.3	0.4	21.2
99.9	12.1	101.2	100.8	100.6	100.4	0.5	24.4
99.9	16.5	101.7	101.2	100.8	100.5	0.6	27.5
99.9	21.4	102.3	101.6	101.2	100.9	1.0	21.4
99.9	34.6	103.9	102.8	102.1	101.5	1.6	21.6
99.9	48.9	105.7	104.2	103.0	102.1	2.2	22.2
99.9	66.3	107.6	105.6	104.0	102.8	2.9	22.8
99.9	86.0	110.0	107.4	105.2	103.6	3.7	23.2
99.9	135.8	111.8	111.5	108.0	105.3	5.4	25.1
99.9	196.6	122.2	116.2	111.0	106.9	7.1	27.7
99.9	135.5	116.0	111.7	108.0	105.1	5.2	26.1
100.0	85.9	110.4	107.8	105.5	103.7	3.7	23.2
99.9	66.2	108.1	106.0	104.4	103.2	3.3	20.1
99.9	49.0	106.1	104.5	103.3	102.4	2.5	19.6
99.9	34.4	104.3	103.2	102.4	101.8	1.9	18.1
99.9	21.3	102.6	101.9	101.4	101.0	1.1	19.4
99.9	16.5	101.9	101.4	101.0	100.7	0.8	20.7
99.9	12.1	101.2	100.9	100.7	100.5	0.6	20.2
99.9	8.5	101.0	100.7	100.5	100.3	0.4	21.3
99.9	5.5	100.8	100.6	100.4	100.2	0.3	18.3

Table 7. Data for the first pool boiling curve for enhanced Surface No. 2 (plotted in Figure 25).

T_{sat} (C°)	q (kW/m ²)	T_{10} (C°)	T_6 (C°)	T_2 (C°)	T_w (C°)	ΔT $= T_w - T_{\text{sat}}$	$h = \frac{q}{\Delta T}$ (kW/m ² -C°)
100.2	5.1	100.4	100.3	100.3	100.3	0.1	50.8
100.1	12.7	100.8	100.9	100.6	100.3	0.2	63.6
100.1	22.3	101.7	101.6	101.1	101.5	0.6	37.2
100.1	37.0	102.6	102.2	101.6	100.9	0.8	46.3
100.1	49.0	103.4	102.8	101.9	101.0	0.9	54.3
100.1	65.0	104.6	103.7	102.5	101.4	1.3	50.0
100.1	85.3	106.0	104.8	103.2	101.6	1.5	56.9
100.1	110.7	107.7	106.0	104.1	102.2	2.1	52.7
100.1	131.0	108.9	106.8	104.6	102.4	2.4	54.6
100.1	191.7	112.6	109.4	106.1	102.9	2.9	66.1
100.1	137.0	109.6	107.3	104.9	102.5	2.4	57.1
100.1	109.2	107.9	106.2	104.2	102.3	2.2	49.6
100.0	84.3	106.4	105.1	103.6	102.1	2.1	40.1
100.0	69.3	105.4	104.4	103.2	102.0	2.0	34.7
100.0	51.4	104.2	103.5	102.6	101.6	1.6	32.1
100.0	35.9	103.1	102.8	102.0	101.2	1.2	30.0
100.0	22.5	102.2	102.0	101.6	101.2	1.2	18.8
100.1	12.2	101.6	101.5	101.2	100.9	0.8	15.3
100.1	6.3	100.6	100.6	100.4	100.2	0.1	63.1

Table 8. Data for the second pool boiling curve for enhanced Surface No. 2 (plotted in Figure 26).

T_{sat} (C°)	q (kW/m ²)	T_{10} (C°)	T_6 (C°)	T_2 (C°)	T_w (C°)	ΔT $= T_w - T_{\text{sat}}$	$h = \frac{q}{\Delta T}$ (kW/m ² -C°)
100.2	5.7	100.4	100.3	100.3	100.3	0.1	57.0
100.2	12.3	100.8	100.8	100.6	100.4	0.2	61.5
100.2	21.7	101.6	101.6	101.1	100.6	0.4	54.3
100.1	35.0	102.5	102.2	101.5	100.8	0.7	47.0
100.1	49.6	103.4	102.9	102.0	101.1	1.0	49.6
100.1	66.9	104.6	103.7	102.5	101.3	1.2	55.7
100.1	86.5	105.8	104.5	103.0	101.5	1.4	61.8
100.1	107.1	107.3	105.5	103.7	101.9	1.8	59.5
100.2	132.2	108.9	106.7	104.4	102.1	1.9	69.6
100.2	195.6	113.1	109.8	106.4	103.0	2.8	69.9
100.2	132.6	109.3	107.1	104.8	102.5	2.3	57.7
100.2	110.0	107.9	106.2	104.2	102.2	2.0	55.0
100.2	89.0	106.7	105.4	103.7	102.0	1.8	49.4
100.2	67.0	105.2	104.4	103.0	101.6	1.4	47.9
100.2	50.4	104.2	103.6	102.5	101.4	1.2	42.0
100.2	34.7	103.0	102.7	102.0	101.3	1.1	31.6
100.2	22.8	102.2	102.2	101.6	101.0	0.8	28.5
100.2	12.5	101.4	101.4	101.1	100.8	0.6	20.9
100.2	5.7	100.4	100.4	100.3	100.2	—	—

Appendix B

Errors involved in the measurements

A digital temperature readout device was used which read temperature to one tenth of a degree ($^{\circ}\text{C}$). At lower heat fluxes when ΔT was of the order of 0.1 to 0.3 $^{\circ}\text{C}$ an error of up to 100% could be involved.

At higher heat fluxes the temperature gradient in the test section below the test surface is not quite linear due to the effect of the electric heater bolt hole; thus, the two thermocouples nearest the test surface are used for extrapolation purposes. The radial conduction heat losses to the outer section of the test surface tend to increase at higher temperatures but the higher boiling heat transfer coefficient from the test surface reduces its thermal resistance correspondingly. Total heat losses were estimated to be about 5% over the heat flux range at which experiments were performed. Therefore, the error should not be significantly high. It should be noted that for comparison purposes the two surfaces (i.e., a smooth surface vs enhanced) are of the same design and hence their errors are similar.

LIST OF REFERENCES

LIST OF REFERENCES

1. Webb, R.L., The Evolution of Enhanced Surface Geometries for Nucleate Boiling, Heat Transfer Engineering, Vol. 2, No. 3-4, pp. 46-69, 1981.
2. Jakob, M., Heat Transfer, Wiley, New York, pp. 636-638, 1949.
3. Kurihari, H.M. and Myers, J.E., Effects of Superheat and Roughness on the boiling Coefficients, AIChE J., Vol. 6, No. 1, pp. 83-91, 1960.
4. Bankoff, S.G., Trans. Am. Soc. Mech. Engrs., 79, 735 (1957).
5. Westwater, J.W., Clark, H.B., and Strange, P.S., Chem. Eng. Progr. Symp. Ser. No. 29, 55, 103 (1959).
6. Griffith, P., and Wallis, J.D., The Role of Surface Conditions in Nucleate Boiling, Chem. Eng. Prog. Symp. Ser., Vol. 55, No. 49, pp. 49-63, 1959.
7. Marto, P.J., and Rohsenow, W.M., Effects of Surface Conditions on Nucleate Pool Boiling of Sodium, J. Heat Transfer, Vol. 88, pp. 196-204, 1966.
8. Hummel, R.L., and Young, R.K., Improved Nucleate Heat Transfer, Chem. Eng. Prog. Symp. Ser., Vol. 61, No. 59, pp. 264-470, 1965.
9. Rohsenow, W.M., and Clark, J.A., idid., 73, 609 (1951).
10. Jakob, Max, "Heat Transfer", Vol. 1, p. 614 Wiley, New York.
11. Forster, K. and Grief, R., Trans. Am. Soc. Mech. Engrs., J. Heat Transfer, 81, 43 (1959).
12. Edwards, D.K., M.S, Thesis, Univ. of Calif., Berkeley, California (1956).
13. Moore, F.D. and Mesler, R.B., The Measurement of Rapid Surface Temperature Fluctuation during Nucleate Boiling of Water, AIChE J., Vol. 7, No. 4, pp. 620-624, 1971.
14. Gottzmann, C.F., Wulf, J.B., and O'Neill, P.S., Theory and Application of High Performance Boiling Surfaces to Components of Absorption Cycle Air Conditioners, Proc. Conf. Nat'l. Gas Res. Tech., Session V, paper 3, Chicago, February 28, 1971.

15. Bergles, A.E. and Chyu, M.C., Characteristics of Nucleate Pool Boiling From Porous Metallic Coatings, Advances in Enhanced Heat Transfer, 1981, HTD-Vol. 18.
16. Yilmaz, S. and Westwater, J.W., Effect of Commercial Enhanced Surfaces on the Boiling Heat Transfer Curve, 20th Nat'l Heat Transfer Conf., Milwaukee AIChE Paper, August 2-5, 1981.
17. Nakayama, W., Daikoku, R., Nakajima, T., Dynamic Model of Enhanced Boiling Heat Transfer on Porous Surfaces Part I,II, ASME J. of Heat Transfer, Vol. 102, No. 3, 1980, pp. 445-456.
18. L'Ecuyer, M.R.L., and Murtby, S.N.B., "Energy Transfer from a liquid to Gas Bubbles Forming at a Submerged Orifice", NASA TN D-2547, 1965.
19. Arshad, J. and Thome, J.R., "Enhanced Boiling Surfaces: Heat Transfer Mechanism and Mixture Boiling", Submitted for the ASME-JSME Thermal Engineering Joint Conference, Honolulu, March 1983.
20. Thome, J.R., "Prediction of Binary Mixture Boiling Heat Transfer Coefficient Using Only Phase Equilibrium Data; accepted for publication by Int. J. Heat Mass Transfer.

MICHIGAN STATE UNIVERSITY LIBRARIES



3 1293 03082 4464